

A&A manuscript no.

(will be inserted by hand later)

Your thesaurus codes are:

06(08.05.3; 08.14.1; 08.16.6; 08.18.1; 02.04.1; 02.05.2)

ASTRONOMY
AND
ASTROPHYSICS

Properties of non-rotating and rapidly rotating protoneutron stars

Klaus Strobel, Christoph Schaab, and Manfred K. Weigel

Sektion Physik, Ludwig-Maximilians Universität, Am Coulombwall 1, D-85748 Garching, Germany

Received 15 December 1998 / Accepted 28 July 1999

Abstract. Properties of non-rotating and rapidly rotating protoneutron stars and neutron stars are investigated. Protoneutron stars are hot, lepton rich neutron stars which are formed in Type-II supernovae. The hot dense matter is described by a realistic equation of state which is obtained by extending a recent approach of Myers and Świątecki to the nuclear mass formula. We investigate the properties of protoneutron stars and neutron stars at different evolutionary stages in order to emphasize the differences between very young and old neutron stars. The numerical calculations are performed by means of an exact description of rapid, uniform rotation in the framework of general relativity. We show that the minimal marginally stable protoneutron star mass is much higher than the corresponding minimum mass of a cold neutron star. The minimum gravitational (baryonic) mass of $0.89 - 1.13 M_{\odot}$ ($0.95 - 1.29 M_{\odot}$) of a neutron star is therefore determined at the earliest stages of its evolution. We also show that the use of different temperature profiles in the envelope as well as different shapes of the neutrino sphere change the properties of protoneutron stars and hot neutron stars by up to 20 %. A preliminary analysis indicates that even the most massive protoneutron stars rotating with Kepler frequency are secularly stable. Under the assumption of conserved angular momentum and baryonic mass, the maximum rotational frequency of an evolved neutron star is determined by the Kepler frequency of the protoneutron star. We can thus derive a lower limit, $P_{\min} \sim 1.56 - 2.22$ ms, to the rotational period of young neutron stars with a canonical gravitational mass of $1.35 M_{\odot}$. This result further supports the assumption that millisecond pulsars are accelerated due to accretion onto a cold neutron star.

Key words: Stars: evolution – Stars: neutron – Stars: pulsars – Stars: rotation – Dense matter – Equation of state

1. Introduction

It is generally believed that a neutron star (NS) is born as a result of the gravitational collapse of the iron core of a massive evolved progenitor star ($M \sim 8 - 25 M_{\odot}$) in a Type-II supernova (e.g. Bethe 1990). The iron core of such a star collapses when its mass reaches the Chandrasekhar limit

$$M_{\text{Ch}} \sim 5.8 Y_e^2 M_{\odot} \sim 1.2 \dots 1.5 M_{\odot}, \quad (1)$$

where Y_e denotes the number of electrons per baryon which depends on the mass of the progenitor star. Due to the Fermi pressure of the nucleons, the collapse stops when nuclear matter density is reached and the core bounces back. Shortly after core bounce (some 10 ms) a hot, lepton rich NS, called *protoneutron* star (PNS), is formed. This PNS consists of a shocked envelope with an entropy per baryon¹ $s \sim 4 - 10$ and an unshocked core with $s \sim 1$ (Burrows et al. 1995). The envelope and the core contain nearly the same mass of about $0.6 - 0.8 M_{\odot}$ (slightly depending on the mass of the progenitor star, see Burrows et al. 1995; Keil et al. 1996). During the so-called Kelvin-Helmholtz cooling phase (e.g. Janka 1993) the lepton number decreases in the PNS due to the loss of neutrinos and consequently the PNS evolves in about 10 to 30 seconds into a hot, lepton poor neutron star (HNS) with an entropy per baryon, $s \sim 1 - 2$, depending on the model (e.g. Burrows & Lattimer 1986; Keil & Janka 1995; Sumiyoshi et al. 1995; Pons et al. 1999). After several minutes this HNS cools to a cold neutron star (CNS) with temperatures $T < 1$ MeV throughout the star (e.g. Keil & Janka 1995). Finally, it slowly cools via neutrino and photon emission until its thermal radiation is too weak to be observable after about 10^7 yr (e.g. Tsuruta & Cameron 1966; Schaab et al. 1996).

The PNS is in β -equilibrium during its lifetime, since the time scale of the weak-interaction is much smaller than the evolutionary time scale, i.e. the neutrino diffusion time scale or the neutrino cooling time scale, respectively. Hence the evolution of a PNS can be studied by considering quasi-stationary models at different times.

Send offprint requests to: K. Strobel,
e-mail: kstrobel@laser.physik.uni-muenchen.de

¹ $k_B = \hbar = c = 1$ throughout this paper.

The properties of PNS's were investigated by different authors. For example, the case of non-rotating PNS's was studied by Takatsuka et al. (1994), Bombaci et al. (1995), and Prakash et al. (1997). The case of rotating PNS's was treated by Romero et al. (1992) and Takatsuka (1995, 1996) by means of an empirical formula for the Kepler frequency which was developed for CNS's (e.g. Haensel et al. 1995). Hashimoto et al. (1994) and Goussard et al. (1997) account for rapid rotation by using an exact, general relativistic approach. Finally, Goussard et al. (1998) have performed the case of differential rotation of PNS's. Most of these authors did not utilize an equation of state (EOS) of hot matter throughout the whole star (except Romero et al. 1992; Goussard et al. 1997, 1998), but used an EOS of cold matter for the envelope of the star instead. As we will show, this simplification leads to radii (Kepler frequencies) which are too small (large).

The aim of this work is to study the properties of non-rotating and rapidly, uniformly rotating PNS's. We use an exact, general relativistic approach to rapid rotation (Schaab 1998). The hot dense matter is described by a recently developed EOS (Strobel et al. 1999), which is based on a modern parametrisation of the Thomas-Fermi approach for finite nuclei and cold nuclear matter performed by Myers & Świątecki (1990, 1991, 1996). We generalize this approach to hot dense matter by taking the thermal effects on both the kinetic and the interaction energy into account. In this way, we construct a set of EOS's with different profiles of the entropy per baryon and different lepton numbers. We can follow the evolution of the PNS into a CNS, by means of this set, at different evolutionary stages. We also investigate the influence of the location and the shape of the neutrino sphere as well as the influence of the value of the temperature in the star's envelope.

The paper is organized as follows. Firstly, in Sect. 2 we will briefly review the physics in the interior of PNS's and describe the different evolutionary stages of PNS's and NS's. Furthermore, we discuss the location and the shape of the neutrino sphere. The EOS's of PNS and NS matter are described in Sect. 3, where we emphasize the influence of finite temperature and trapped lepton number. The properties of rotating and non-rotating PNS's and NS's are presented in Sect. 4. Finally, discussion of our results and conclusions are given in Sect. 5.

2. Inside a protoneutron star

A PNS differs in several respects from a CNS: At the beginning of its lifetime the PNS contains a high lepton number, Y_l , since the core is opaque with respect to neutrinos. A further difference is the high temperature which cannot be neglected with respect to the Fermi temperature throughout the whole PNS. We define, as usual, the lepton number, $Y_l = Y_e + Y_{\nu_e}$, as the sum of the net electron fraction, $Y_e = (n_{e^-} - n_{e^+})/n$, (where n , n_{e^-} , and n_{e^+} are the baryon number density, the electron number density,

and the positron number density, respectively) and the net electron neutrino fraction, $Y_{\nu_e} = (n_{\nu_e} - n_{\bar{\nu}_e})/n$, (where n_{ν_e} and $n_{\bar{\nu}_e}$ are the electron neutrino number density and the electron anti-neutrino number density, respectively). Since the muon number density is small in a PNS, they are neglected here. The reason for the small muon number is that the muon lepton family number is conserved, $Y_\mu + Y_{\nu_\mu} = 0$, while the neutrinos are trapped². Relativistic calculations lead to the conclusion that NS's and PNS's are composed not only of nucleons and leptons but also of hyperons and, possibly, of nucleon isobars (see, e.g. Pandharipande 1971; Schaffner & Mishustin 1996; Balberg & Gal 1997; Huber et al. 1998). Nevertheless, we shall not take these particle species into account. In view of the rather large uncertainties of the hyperon couplings, we shall, as a first approach to this problem, neglect these additional degrees of freedom. In the following we select four different stages in the evolution of PNS's and NS's, namely at times $t_1 \sim 50 - 100$ ms, $t_2 \sim 0.5 - 1$ s, $t_3 \sim 10 - 30$ s, and $t_4 =$ some minutes after core bounce.

2.1. Protoneutron stars about 50 - 100 ms after core bounce

This early type protoneutron star (EPNS) is characterized by a hot shocked envelope with an entropy per baryon of $s \sim 4 - 5$ for densities $n < 0.02 \text{ fm}^{-3}$, an unshocked core with $s \sim 1$ for densities $n > 0.1 \text{ fm}^{-3}$, and a transition region between these densities (Burrows et al. 1995). The entropy per baryon in the very outer layers of an EPNS is larger than $s \sim 10$. However, these layers have only a small influence on the EPNS structure and are therefore neglected. We investigate EPNS models with constant lepton number, $Y_l = 0.4$ for densities above $n = 6 \times 10^{-4} \text{ fm}^{-3}$ where the neutrinos are trapped (Burrows et al. 1995). Below this density, the neutrinos can freely escape and the chemical potential of the neutrinos vanishes, $\mu_{\nu_e} = 0$ (Cooperstein 1988). We refer to Table 1 for the detailed parameters of the EPNS models studied here.

2.2. Protoneutron stars at $t \sim 0.5 - 1$ s after core bounce

At this later stage, the entropy per baryon is approximately constant throughout the star, $s \sim 2$, except in some outer regions (Burrows & Lattimer 1986; Keil & Janka 1995; Keil 1996). The lepton number is approximately constant since the neutrino diffusion time, $\tau_{\nu\text{-diff}} \sim 10$ s, is by an order of magnitude larger than the PNS's age. We model this late type protoneutron star (LPNS) with a neutrino transparent envelope with densities $n < n_{\text{env}} = 6 \times 10^{-4} \text{ fm}^{-3}$ and a neutrino opaque core

² This statement is also true for massive neutrinos recently detected by the Super-Kamiokande collaboration (see Fukuda et al. 1998). The detected mass is too small to allow considerable flavour oscillations during the first seconds of a supernova (see discussion in Section 9.5.3 of Raffelt 1996)

Table 1. Entropies, temperatures, densities, and lepton numbers used in this paper. The entries are: entropy per baryon or temperature in the envelope, $s_{\text{env}}, T_{\text{env}}$; entropy per baryon or temperature in the core, $s_{\text{core}}, T_{\text{core}}$; maximum baryon number density of the envelope correlated with the entropy per baryon or temperature in the envelope, $n(s_{\text{env}}, T_{\text{env}})$; minimum baryon number density of the core correlated with the entropy per baryon or temperature in the core, $n(s_{\text{core}}, T_{\text{core}})$; baryon number density below which the neutrinos are not trapped, $n(Y_{1,\text{env}})$; baryon number density above which the neutrinos are totally trapped, $n(Y_{1,\text{core}})$; lepton fraction inside the core, $Y_{1,\text{core}}$.

Label	$s_{\text{env}}, T_{\text{env}}$	$s_{\text{core}}, T_{\text{core}}$	$n(s_{\text{env}}, T_{\text{env}})$ [fm ⁻³]	$n(s_{\text{core}}, T_{\text{core}})$ [fm ⁻³]	$n(Y_{1,\text{env}})$ [fm ⁻³]	$n(Y_{1,\text{core}})$ [fm ⁻³]	$Y_{1,\text{core}}$
EPNS _{YL04} ^{s5s1}	5.0	1.0	0.02	0.1	0.0006	0.0006	0.4
EPNS _{YL04} ^{s4s1}	4.0	1.0	0.02	0.1	0.0006	0.0006	0.4
LPNS _{YL04} ^{s2}	2.0	2.0	-	-	0.0006	0.0006	0.4
LPNS _{YL04} ^{T06s2}	0.6 MeV	2.0	0.0004	0.0004	0.0006	0.0006	0.4
LPNS _{YL04} ^{s2} *	2.0	2.0	-	-	0.0006	0.006	0.4
LPNS _{YL04} ^{s2} (64–63)	2.0	2.0	-	-	0.0006	0.02	0.4
LPNS _{YL04} ^{s2} (64–22)	2.0	2.0	-	-	0.0006	0.06	0.4
LPNS _{YL04} ^{s2} (64–62)	2.0	2.0	-	-	0.0006	0.0006	0.3
LPNS _{YL03} ^{s1}	1.0	1.0	-	-	0.0006	0.0006	0.4
LPNS _{YL03} ^{s1}	1.0	1.0	-	-	0.0006	0.0006	0.3
LPNS _{YL04} ^{s0}	0	0	-	-	0.0006	0.0006	0.4
HNS ^{s2}	2.0	2.0	-	-	-	-	-
HNS ^{T06s2}	0.6 MeV	2.0	0.0004	0.0004	-	-	-
HNS ^{T0s2}	0 MeV	2.0	0.06	0.06	-	-	-
HNS ^{s1}	1.0	1.0	-	-	-	-	-
HNS ^{T03s1}	0.3 MeV	1.0	0.0004	0.0004	-	-	-
HNS ^{T0s1}	0 MeV	1.0	0.06	0.06	-	-	-
CNS	0 MeV	0 MeV	-	-	-	-	-

* This notation means that the first number in parentheses classifies the lower density boundary of the neutrino sphere, i.e. 6×10^{-4} , the second number gives the upper density boundary, i.e. 6×10^{-3} .

with densities $n > n_{\text{core}}$ and $Y_1 = 0.4$ (see Table 1). The transition region between n_{env} and n_{core} is called *neutrino sphere* (Janka 1993). We choose four different values for n_{core} to simulate the influence of the shape of the neutrino sphere on the structure of LPNS's. We show also a LPNS with $Y_1 = 0.3$ for densities $n > 6 \times 10^{-4} \text{ fm}^{-3}$, for the sake of comparison, since different evolution calculations show different lepton numbers (Burrows & Lattimer 1986; Keil & Janka 1995; Pons et al. 1999).

These different choices are motivated by recent theoretical calculations of the neutrino-nucleon cross-section that include modifications due to the nucleon-nucleon interaction and spin-spin correlations. The problem was treated, for instance, by Raffelt (1996), Reddy et al. (1998), Burrows & Sawyer (1998), and Pons et al. (1999) using static correlation functions and by Raffelt (1996), Janka et al. (1996), Raffelt & Strobel (1997), and T. Strobel (work in preparation) by using dynamical correlation functions. Because of the high complexity of the problem, the behaviour of the cross section and thus of the loca-

tion and shape of the neutrino sphere is rather uncertain. Another reason for the different choices is the uncertainty due to convection, that might considerably influence the cooling of PNS's (e.g. Burrows & Lattimer 1988; Keil et al. 1996; Mezzacappa et al. 1998).

For the sake of comparison, we investigate also a model with an isothermal envelope with temperature³ $T = 0.6 \text{ MeV}$ for densities below $n \sim 4 \times 10^{-4} \text{ fm}^{-3}$. This temperature value is motivated by the fact that the temperature in the central parts of the progenitor star approximately raises to this value before the onset of the core collapse (e.g. Shapiro & Teukolsky 1983; Bethe 1990). It is certainly an upper limit of the true temperature since it corresponds to an increase of the entropy per baryon by three or four orders of magnitude for densities $n \sim 6 \times 10^{-10} \text{ fm}^{-3}$ (outer most layer of the star). This high entropy

³ We choose T and not T^* for simplicity, because the values of T and T^* are comparable in the envelope; for the definition of T^* , which includes metric corrections, see Goussard et al. (1997) and Gondek et al. (1997).

seems to be possible only in hot bubbles (see Mathews et al. 1993).

For comparison we investigate also an unphysical, cold EOS, $\text{LPNS}_{\text{YL04}}^{\text{s0}}$, with a trapped lepton number of $Y_l = 0.4$ for densities $n > 6 \times 10^{-4} \text{ fm}^{-3}$.

2.3. Deleptonized hot neutron star at $t \sim 10 - 30 \text{ s}$ after core bounce

After $10 - 30 \text{ s}$ the neutrinos can freely escape and the HNS is nearly deleptonized. This also means that the lepton family number is not conserved anymore. The β -equilibrium is thus given by $\mu_p + \mu_e = \mu_n$, $\mu_e = \mu_\mu$, and $\mu_\nu = 0$ for all neutrino species. At this stage muons have to be taken into account since the muon number density is comparable to the electron number density above nuclear matter density. The entropy per baryon is nearly constant, $s \sim 1 - 2$, during the evolution from the LPNS to the HNS (e.g. Burrows & Lattimer 1986; Keil & Janka 1995; Sumiyoshi et al. 1995; Pons et al. 1999).

We again compare the models with isentropic envelopes with models with isothermal envelopes, $T = 0.3 \text{ MeV}$ or $T = 0.6 \text{ MeV}$ for densities below $n \sim 4 \times 10^{-4} \text{ fm}^{-3}$. The models for the deleptonized HNS's are summarized in Table 1.

2.4. Cold neutron star some minutes after core bounce

After some minutes the NS has a temperature of $T < 1 \text{ MeV}$ throughout the star and the EOS for cold NS matter can be used to describe the CNS, because the thermal effects are negligibly small (see Shapiro & Teukolsky 1983). We shall adopt the model derived by Baym et al. (1971) for densities below neutron drip density, $n < 2.6 \times 10^{-4} \text{ fm}^{-3}$, and Negele & Vautherin (1973) for densities between neutron drip density and the transition density, $2.6 \times 10^{-4} < n < 0.1 \text{ fm}^{-3}$. Above this transition density, we use the model for CNS matter in β -equilibrium without neutrinos derived by Strobel et al. (1997).

3. Equation of state for protoneutron stars

The EOS of PNS matter is the basic input quantity whose knowledge over a wide range of densities, ranging from the density of iron at the star's surface up to about eight times the density of normal nuclear matter reached in the cores of the most massive stars of a sequence, is necessary to solve the structure equations. Due to the high lepton number, the EOS of PNS's is different from the EOS's for cold and hot NS's with low lepton numbers. The nuclear EOS used in this paper for the description of a PNS is a Thomas-Fermi model of average nuclear properties, with a momentum- and density-dependent, effective nucleon-nucleon interaction developed by Myers & Świątecki (1990, 1991). The parameters of the nuclear EOS were adjusted to reproduce a wide range of properties

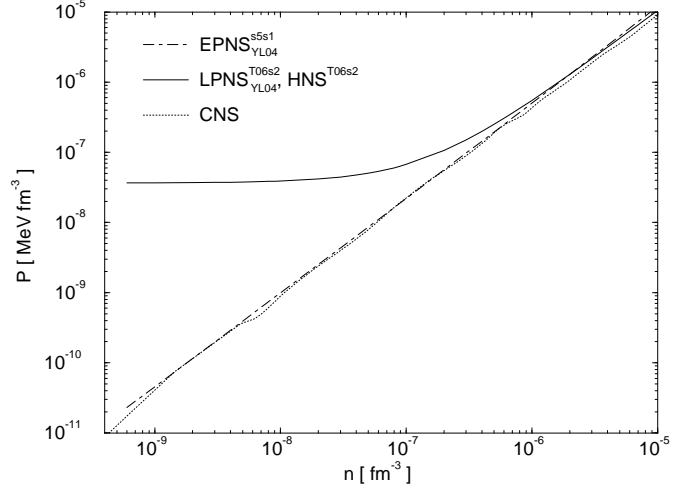


Fig. 1. Pressure versus baryon number density for densities $n < 10^{-5} \text{ fm}^{-3}$ of hot dense matter. The curve CNS corresponds to cold matter (see Sect. 2.4). The $\text{LPNS}_{\text{YL04}}^{\text{T06s2}}$ and $\text{HNS}^{\text{T06s2}}$ curve is the isothermal envelope part of an isentropic core with entropy per baryon $s = 2$ (see Sects. 2.2 and 2.3 for explanation). Finally the curve $\text{EPNS}_{\text{YL04}}^{\text{s5s1}}$ corresponds to the envelope part of this EOS with $s = 5$ and no trapped lepton number in this density region.

of normal nuclear matter and nuclei (Myers & Świątecki 1995, 1996, 1998; Wang et al. 1997). Strobel et al. (1999) extended this approach to the case of finite temperature⁴, where they use exact numerical solutions for the integration over the Fermi-Dirac distribution functions. Appendix A contains a brief description of this approach. We extend the nuclear EOS to subnuclear densities and to different compositions of PNS and HNS matter (i.e. trapped neutrinos, constant entropy per baryon, ...). In the subnuclear regime, the EOS was also obtained by means of the homogeneous Thomas-Fermi model. The electron number is derived by fitting the pressure to the subnuclear EOS's of Baym et al. (1971) and Negele & Vautherin (1973) for densities below the density of the neutrino sphere in the case of EPNS and LPNS models and below the nuclear density in the case of HNS models. Our results for subnuclear densities are comparable to the EOS's derived by Lattimer & Swesty (1991) and used in the investigations of Goussard et al. (1997, 1998) and Gondek et al. (1997).

Figures 1 - 3 show the pressure, $P(n)$, as function of the baryon number density, n , for different physical scenarios. The envelope region with densities, $n \leq 10^{-5} \text{ fm}^{-3}$ is depicted in Fig. 1 for the isothermal part with $T = 0.6$ of the $\text{LPNS}_{\text{YL04}}^{\text{T06s2}}$ EOS and the $\text{HNS}^{\text{T06s2}}$ EOS, the isentropic $\text{EPNS}_{\text{YL04}}^{\text{s5s1}}$ EOS, and the EOS for a CNS. The neutrinos do not contribute to the pressure for densities $n < 6 \times 10^{-4} \text{ fm}^{-3}$, since they are not trapped in this region. In the EOS with $T = 0.6 \text{ MeV}$, the pressure

⁴ The EOS's used in this paper are available at: <http://www.physik.uni-muenchen.de/sektion/suessmann/astro>.

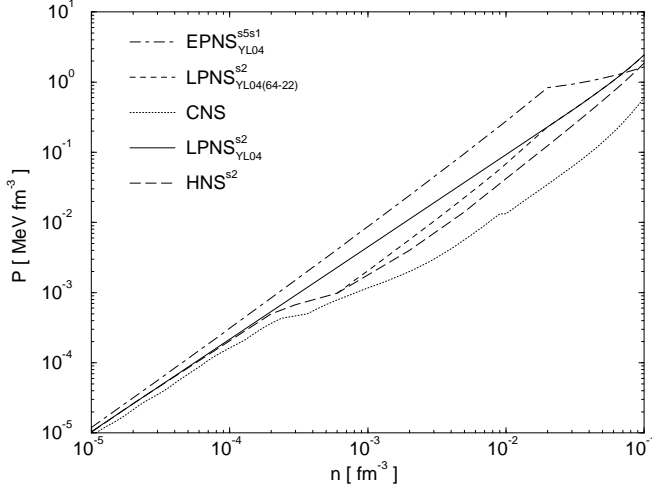


Fig. 2. Pressure versus baryon number density in the density region $10^{-5} \text{ fm}^{-3} < n < 10^{-1} \text{ fm}^{-3}$ for different EOS's of hot dense matter. The abbreviations are described in Table 1.

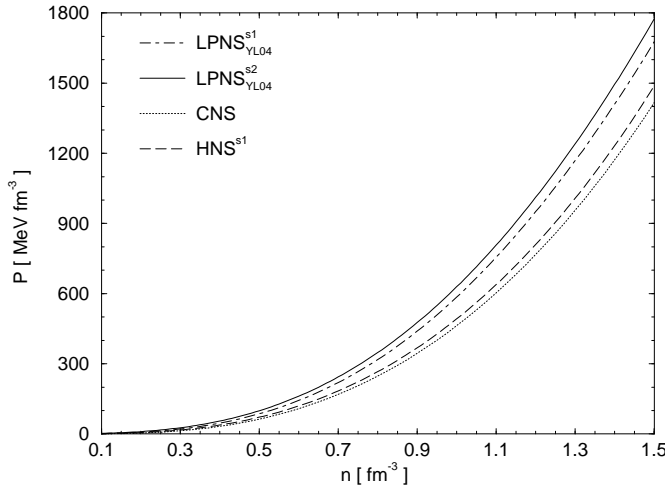


Fig. 3. Pressure versus baryon number density for densities $n > 0.1 \text{ fm}^{-3}$ for different EOS's of our model of hot dense matter. The abbreviations are described in Table 1. The pressure of the HNS^{s1} EOS is nearly identical to the LPNS^{s1}_{YL04} case in this density region and is not shown for that reason.

is dominated by the contribution of the photons, $p_{\text{Ph}} = 2.817 \times 10^{-7} T^4 \text{ MeV}^{-3} \text{ fm}^{-3} = 3.65 \times 10^{-8} \text{ MeV fm}^{-3}$, for low densities. Nevertheless, the influence of this low density region on gross properties of LPNS's and HNS's is only small (see Sect. 4). In contrast to the isothermal EOS, the isentropic EOS is almost identical with the cold EOS in this density region.

Figure 2 shows the general trend that the leptons dominate the pressure in the density region around and above the neutrino sphere, $10^{-4} \text{ fm}^{-3} < n < 10^{-1} \text{ fm}^{-3}$ for LPNS's. Both thermal effects and the trapped lepton number contribute significantly to the pressure and increase it

by a factor of $\sim 3 - 4$ each at $n = 0.01 \text{ fm}^{-3}$. The thermal effects are even larger for the high entropy model labeled EPNS^{s5s1}_{YL04}. The impact of the shape of the neutrino sphere can be inferred by comparison of the curves labeled LPNS^{s2}_{YL04} and LPNS^{s2}_{YL04(64-22)}.

With increasing density the temperature dependence of the nuclear EOS increases. At the highest densities possible in PNS's ($n \sim 1 - 1.2 \text{ fm}^{-3}$) the pressure increase due to thermal effects and due to high lepton numbers become comparable (see Fig. 3). This feature is clearly expressed by the nearly identical pressure of the HNS^{s2} and the LPNS^{s1}_{YL04} EOS's.

The EOS of Lattimer & Swesty (1991) shows a smaller temperature dependence at high densities (see Goussard et al. 1997) in comparison with our EOS. The reason for this is that the temperature dependence of the EOS of Lattimer & Swesty (1991) lies entirely in the kinetic part of the energy density, since they choose $m^* = m$ in their approach⁵. At this point it should be mentioned, that the behaviour of m^* at high densities is highly uncertain. At $n \sim 0.5 \text{ fm}^{-3}$ we obtain, for instance, a pressure increase due to thermal effects of 28 % (from the LPNS^{s0}_{YL04} to the LPNS^{s2}_{YL04} case), whereas Lattimer & Swesty (1991) obtain an increase of only 8 % (see Fig. 1.b in Goussard et al. 1997). The impact on the structure of PNS's and HNS's are discussed in Section 4, where we compare our results with the results of Goussard et al. (1997, 1998) and Gondek et al. (1997) who used the EOS of Lattimer & Swesty (1991).

The number density and the mean energy of the neutrinos $y = \nu_e, \bar{\nu}_e, \nu_\mu, \bar{\nu}_\mu, \nu_\tau, \bar{\nu}_\tau$ are given by⁶:

$$n_y = \frac{g}{2\pi^2} \int_0^\infty \frac{p^2}{1 + \exp(\frac{1}{T}(p - \mu_y))} dp \quad (2)$$

and

$$u_y = \frac{g}{2n_y\pi^2} \int_0^\infty \frac{p^3}{1 + \exp(\frac{1}{T}(p - \mu_y))} dp, \quad (3)$$

respectively. The trapped electron neutrinos and anti-neutrinos are in chemical equilibrium, $\mu_{\bar{\nu}_e} = -\mu_{\nu_e}$. The chemical potentials of all other neutrino species vanish, $\mu_x = 0$ (with $x = \nu_\mu, \bar{\nu}_\mu, \nu_\tau, \bar{\nu}_\tau$) due to the lepton family number conservation (the muon number density is small compared to the electron number density in PNS's and is therefore neglected, for simplicity). The factor g denotes the spin-degeneracy factor and is related to the spin, s , of the particles by $g = 2|s| + 1$. Since only positive helicity neutrinos and negative helicity anti-neutrinos exist⁷, the

⁵ See Sect. 2.3 of Lattimer & Swesty (1991), especially Eqs. 2.8, 2.13, and 2.18. This will change if m^* is chosen to be smaller than m .

⁶ The recently detected mass of neutrinos (see Fukuda et al. 1998) is much smaller than the mean energy of the neutrinos. A finite neutrino mass therefore can be neglected.

⁷ No negative helicity neutrinos nor positive helicity anti-neutrinos were found in experiment until now; CP violation of the weak interaction.

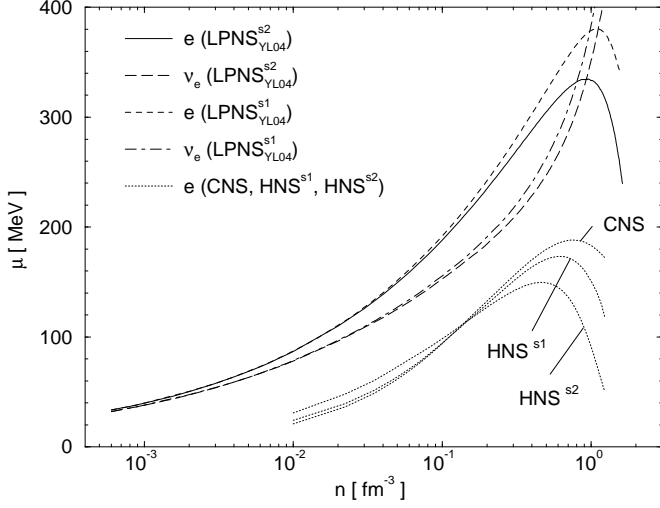


Fig. 4. Chemical potential versus baryon number density for electrons and electron-neutrinos of the $\text{LPNS}_{\text{YL04}}^{\text{s1}}$ and $\text{LPNS}_{\text{YL04}}^{\text{s2}}$ cases. The dotted lines correspond to the CNS, the HNS^{s1} and the HNS^{s2} EOS's.

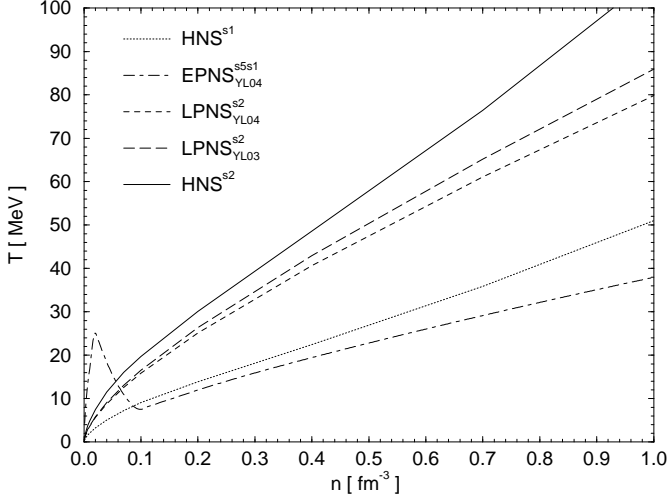


Fig. 5. Temperature versus baryon number density for different EOS's.

degeneracy factor is equal 1 for the neutrinos. In the case of vanishing chemical potential Eqs. (2) and (3) lead to a temperature dependence of the number density:

$$n_x = 1.19 \times 10^{-8} T^3 \text{ MeV}^{-3} \text{ fm}^{-3} \quad (4)$$

and a linear temperature dependence of the mean neutrino energy:

$$u_x = 3.15 T, \quad (5)$$

with $x = \nu_\mu, \bar{\nu}_\mu, \nu_\tau, \bar{\nu}_\tau$. Due to the high chemical potential of the electron neutrinos in the case of a high trapped lepton number ($\mu_{\nu_e} \gg T$; see Fig. 4 and Fig. 5), the number density and the mean energy of the electron anti-neutrinos can be approximated by:

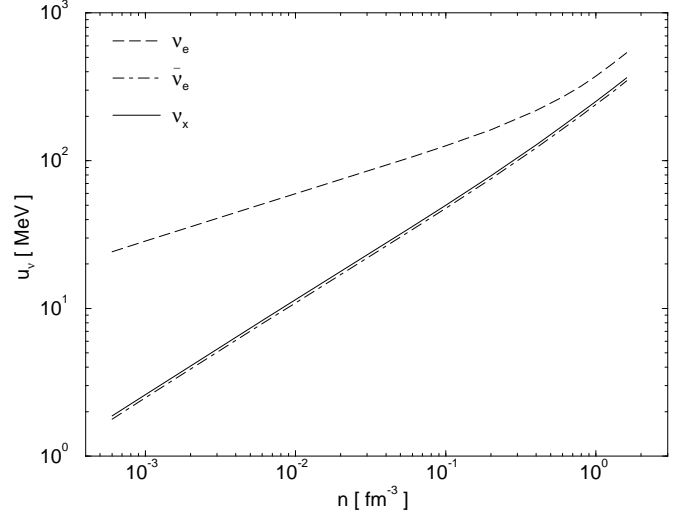


Fig. 6. Mean neutrino energies versus baryon number density for all neutrino types in the case $\text{LPNS}_{\text{YL04}}^{\text{s2}}$ for densities larger than $6 \times 10^{-4} \text{ fm}^{-3}$ ($\nu_x = \nu_\mu, \bar{\nu}_\mu, \nu_\tau$ and $\bar{\nu}_\tau$).

$$n_{\bar{\nu}_e} = \frac{T^3}{\pi^2} \exp\left(-\frac{\mu_{\nu_e}}{T}\right) \quad (6)$$

and

$$u_{\bar{\nu}_e} = \frac{3T^4}{n_{\bar{\nu}_e} \pi^2} \exp\left(-\frac{\mu_{\nu_e}}{T}\right). \quad (7)$$

This leads to the simple, linear temperature dependence of the mean energy of the electron anti-neutrinos:

$$u_{\bar{\nu}_e} = 3T, \quad (8)$$

the energy of an ultra-relativistic Boltzmann gas. The mean neutrino energies of all neutrino species are shown in Fig. 6 for the case $\text{LPNS}_{\text{YL04}}^{\text{s2}}$. Figure 4 shows the chemical potential of the electron neutrinos and the electrons for different models of the EOS.

In Fig. 5 we show the density dependence of the temperature for different EOS's. One can see the temperature drop in the $\text{EPNS}_{\text{YL04}}^{\text{s5s1}}$ EOS at the interface between the hot shocked envelope ($n < 0.02 \text{ fm}^{-3}$) and the unshocked core ($n > 0.1 \text{ fm}^{-3}$) (see Burrows & Lattimer 1986; Burrows et al. 1995). The temperature increases with increasing entropy per baryon (see discussion in Sect. 4.2) and decreases with increasing lepton number, since the neutron fraction and the proton fraction become more equal (see Prakash et al. 1997). The maximum temperature in the most massive PNS's and HNS's reaches values between 80 and 120 MeV (see Fig. 5 and Table 5). The temperature in PNS's and HNS's with a typical baryonic mass of $1.5M_\odot$ has values between 20 and 40 MeV (see Table 3).

The fractions of electrons and electron-neutrinos are shown in Fig. 7 for the $\text{LPNS}_{\text{YL04}}^{\text{s1}}$ and $\text{LPNS}_{\text{YL04}}^{\text{s2}}$ cases with constant lepton number. The lepton fractions of the unphysical $\text{LPNS}_{\text{YL04}}^{\text{s0}}$ EOS are nearly identical to that of the $\text{LPNS}_{\text{YL04}}^{\text{s1}}$ EOS and are not shown in Fig. 7 for

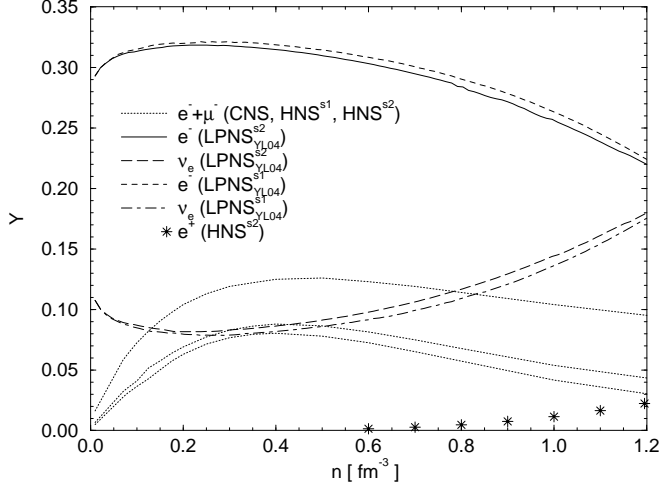


Fig. 7. Lepton fractions versus baryon number density for different EOS's. The lepton fractions of the unphysical $\text{LPNS}_{\text{YL04}}^0$ EOS are nearly identical to that of the $\text{LPNS}_{\text{YL04}}^{\text{s1}}$ EOS and is not shown for that reason. The lower dotted line corresponds to the CNS EOS, the middle dotted line to the HNS^{s1} EOS and the upper dotted line to the HNS^{s2} EOS. The dotted lines show the sum of the electron and muon fraction. The stars correspond to the positron fraction of the HNS^{s2} case. The positron fraction of all other EOS's lies below the resolution of this figure.

that reason. The fractions are nearly constant (29 – 32% for electrons and 8 – 11% for electron neutrinos) in a wide range of densities. The electron fraction decreases for $n > 0.7 \text{ fm}^{-3}$ since the symmetry energy decreases for densities $n > 0.4 \text{ fm}^{-3}$ (Strobel et al. 1997). Non-relativistic EOS's derived within variational approaches behave similar in this respect, whereas the symmetry energy derived in relativistic and non-relativistic Brückner-Bethe calculations monotonically increases with density (see Strobel et al. 1997). Higher temperatures cause a small decrease (increase) of the electron (electron neutrino) fraction (see Takatsuka et al. 1994). Without trapped neutrinos the sum of the electron and muon fraction increases, in first approximation, quadratically with increasing temperature (see Fig. 7 and Keil & Janka 1995).

The effective masses, m_τ^*/m_τ , of neutrons and protons for symmetric and pure neutron matter are shown in Fig. 8. The effective mass for symmetric nuclear matter at saturation density is found to be $m_\tau^*/m_\tau = 0.867$ for neutrons and protons in our model. This is in good agreement with the generally accepted, experimental value (e.g. Bauer et al. 1982). In the case of pure neutron matter, the effective neutron mass increases up to $m_n^*/m_n = 0.935$, at nuclear matter density, whereas the effective proton mass in pure neutron matter decreases to $m_p^*/m_p = 0.808$.

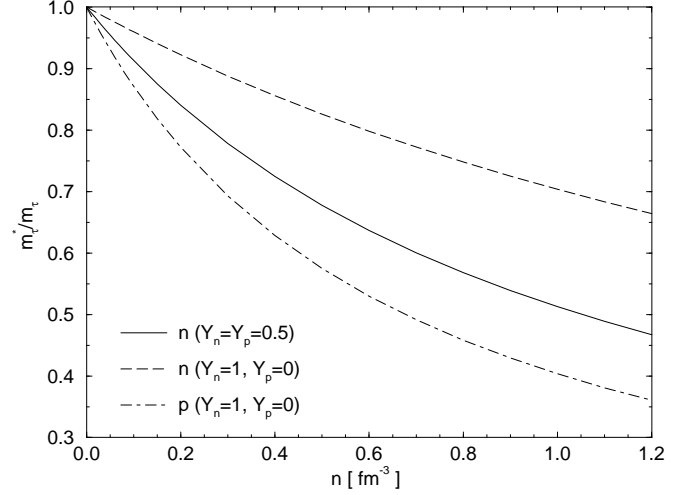


Fig. 8. Effective mass of neutrons and protons versus baryon number density. The solid line shows the effective mass of neutrons and protons for symmetric nuclear matter (the difference in the values for neutrons and protons are negligibly small). The long dashed line shows the effective mass of neutrons in pure neutron matter. The dot-dashed line shows the effective mass of protons brought into pure neutron matter.

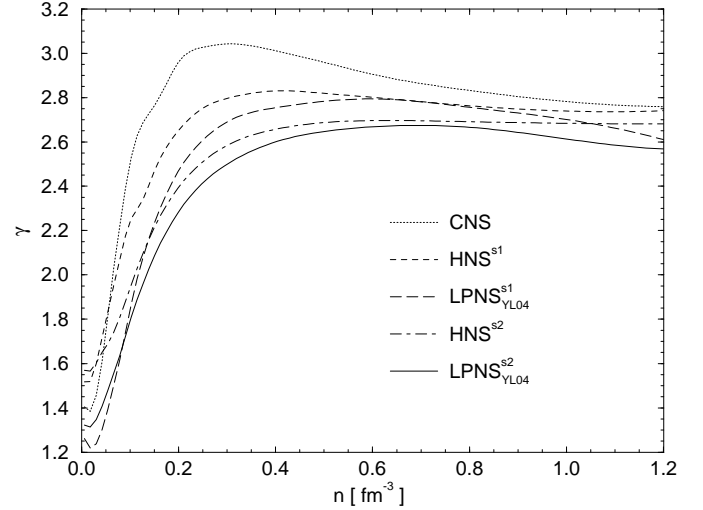


Fig. 9. Adiabatic index versus baryon number density for different EOS's.

The adiabatic index γ :

$$\gamma = \left. \frac{d \ln P}{d \ln n} \right|_s = \left. \frac{n}{P} \frac{dP}{dn} \right|_s, \quad (9)$$

is shown for different EOS's in Fig. 9. The adiabatic index decreases with increasing temperature and lepton numbers for densities around and above nuclear density. In contrast, it decreases with increasing lepton number for densities $n < 0.05 \text{ fm}^{-3}$ (see Gondek et al. 1997). The steep behaviour of the adiabatic index γ around nuclear matter

Table 2. The speed of sound v_s in the density region around and above nuclear matter density for different EOS's. The abbreviations are described in Table 1. The maximum value is reached in the CNS EOS: $n_c^{\text{max}}(\text{CNS}) = 1.246 \text{ fm}^{-3} \rightarrow v_s = 0.964$ (in units of c).

EOS	$n \text{ [fm}^{-3}\text{]}$									
	0.02	0.06	0.1	0.2	0.3	0.4	0.6	0.8	1.0	1.2
LPNS _{YL04} ^{s2}	0.1242	0.1627	0.2067	0.3270	0.4411	0.5434	0.7089	0.8276	0.9055	0.9594
LPNS _{YL04} ^{s1}	0.1046	0.1320	0.1737	0.2968	0.4172	0.5240	0.7008	0.8257	0.9113	0.9617
HNS ^{s2}	0.1011	0.1473	0.1917	0.3128	0.4280	0.5305	0.6963	0.8176	0.9073	0.9750
HNS ^{s1}	0.0684	0.1095	0.1559	0.2735	0.3905	0.4962	0.6665	0.7921	0.8862	0.9606
CNS	0.0507	0.0807	0.1255	0.2469	0.3699	0.4802	0.6569	0.7863	0.8812	0.9543

density is the reason for the core bounce of the collapsing iron core of the progenitor star (Shapiro & Teukolsky 1983).

The speed of sound v_s in units of the speed of light c :

$$v_s = \sqrt{\frac{dP}{d\varepsilon}} = \sqrt{\gamma \frac{P}{\varepsilon + P}}, \quad (10)$$

is tabulated in Table 2 for different EOS's. The speed of sound v_s increases with density up to nearly the speed of light, in the most massive stars of a sequence. Nevertheless, v_s is always smaller than the speed of light and all EOS's used in this paper are causal. The speed of sound increases with temperature and lepton number at fixed density in contrast to the results of Goussard et al. (1998). This is probably caused by the smaller temperature dependence of the EOS of Lattimer & Swesty (1991), which was discussed before in this section.

4. Structure of rotating and non-rotating protoneutron stars

The structure of rotating PNS's and NS's is governed by the Einstein equations in stationary, axisymmetric, and asymptotic flat space-time. Under these special conditions to the space-time symmetry the ten Einstein equations reduce to four non-trivial equations which are elliptic in quasi-isotropic coordinates (Bonazzola et al. 1993). The four non trivial Einstein equations together with the energy-momentum conservation are solved via a finite difference scheme (Schaab 1998). We follow Bonazzola et al. (1993) in compactifying the outer space to a finite region by using the transformation $r \rightarrow 1/r$. The boundary condition of approximate flatness can then be exactly fulfilled. The neutron star model is uniquely determined by fixing one of the parameters: central density, gravitational mass, or baryon number, as well as one of the parameters: angular velocity, angular momentum, or stability parameter $\beta = E_{\text{kin}}/|E_{\text{grav}}|$. The models of maximum mass and/or maximum rotation velocity can also be calculated.

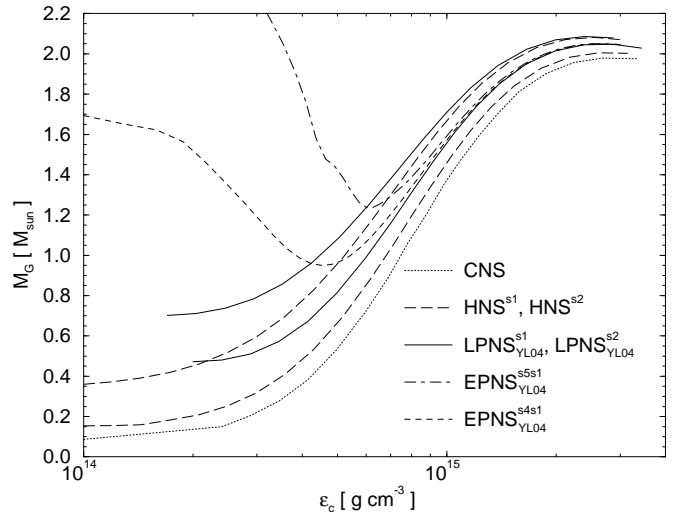


Fig. 10. The gravitational mass versus central energy-density of non-rotating NS's and PNS's. The lower long dashed line corresponds to the HNS^{s1} EOS and the upper long dashed line to the HNS^{s2} EOS. The lower solid line corresponds to the LPNS_{YL04}^{s1} EOS and the upper solid line to the LPNS_{YL04}^{s2} EOS.

4.1. Protoneutron star and neutron star sequences

Figure 10 shows the gravitational mass as function of the central energy-density for the non-rotating PNS and NS models. Only models whose gravitational masses increase with central energy-density are stable against axisymmetric perturbations. Whereas the maximum mass differs only by $\sim 5\%$ between the various star models, the minimum mass of the EPNS models, $M_{\text{min}} \sim 0.9 - 1.2 M_{\odot}$, is much larger than the minimum mass of the CNS models, $M_{\text{min}} \sim 0.1 M_{\odot}$.

Figure 11 shows the Kepler frequency, i.e. the frequency at which mass shedding sets in, as function of the gravitational mass. Also shown is the rotational frequency,

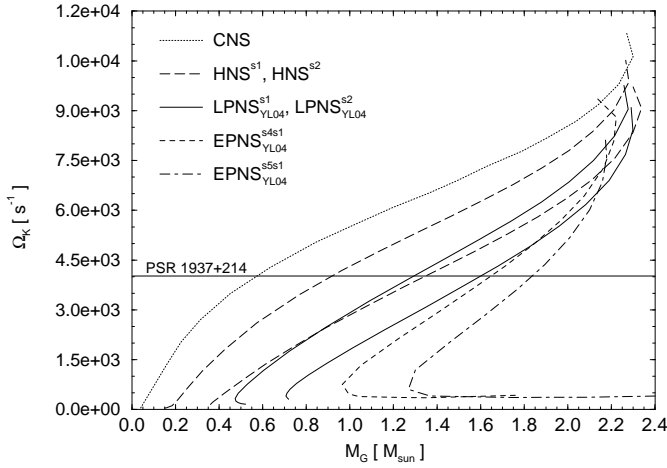


Fig. 11. Kepler frequency versus gravitational mass of PNS's and NS's for different EOS's. The upper long dashed line corresponds to the HNS^{s1} EOS and the lower long dashed line to the HNS^{s2} EOS. The upper solid line corresponds to the $\text{LPNS}_{\text{YL04}}^{\text{s1}}$ EOS and the lower solid line to the $\text{LPNS}_{\text{YL04}}^{\text{s2}}$ EOS.

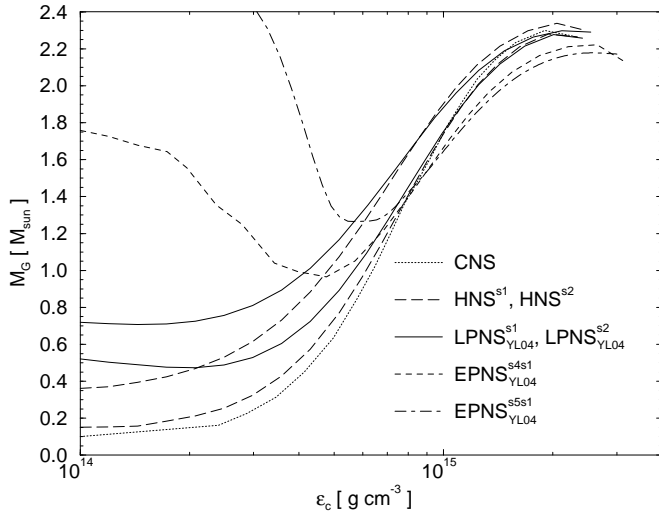


Fig. 12. The gravitational mass versus central energy-density of NS's and PNS's rotating at their Kepler frequency. The lower long dashed line corresponds to the HNS^{s1} EOS and the upper long dashed line to the HNS^{s2} EOS. The lower solid line corresponds to the $\text{LPNS}_{\text{YL04}}^{\text{s1}}$ EOS and the upper solid line to the $\text{LPNS}_{\text{YL04}}^{\text{s2}}$ EOS.

$\Omega = 4033 \text{ s}^{-1}$, of the fastest pulsar known, PSR 1937+214 (Backer et al. 1982). The gravitational mass of this pulsar is unfortunately unknown but is typically assumed to be in the range $1.0\text{--}2.0 M_{\odot}$. Since the Kepler frequency of the CNS models is larger than the rotational frequency of PSR 1937+214 for this mass range, this model is consistent with the observation.

Figure 12 shows the sequences of stars rotating with Kepler frequency. As expected the masses are now larger

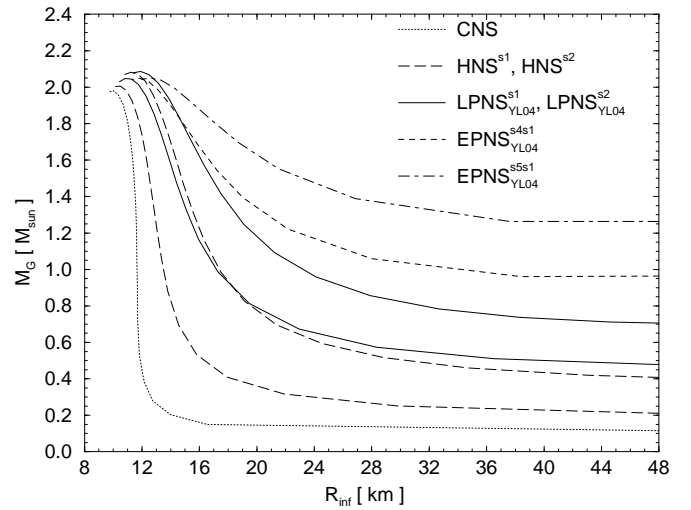


Fig. 13. The gravitational mass versus stellar radius (as measured by an observer located at infinity) of non-rotating NS's and PNS's. The abbreviations for the different EOS's are described in Table 1. The lower long dashed line corresponds to the HNS^{s1} EOS and the upper long dashed line to the HNS^{s2} EOS. The lower solid line corresponds to the $\text{LPNS}_{\text{YL04}}^{\text{s1}}$ EOS and the upper solid line to the $\text{LPNS}_{\text{YL04}}^{\text{s2}}$ EOS.

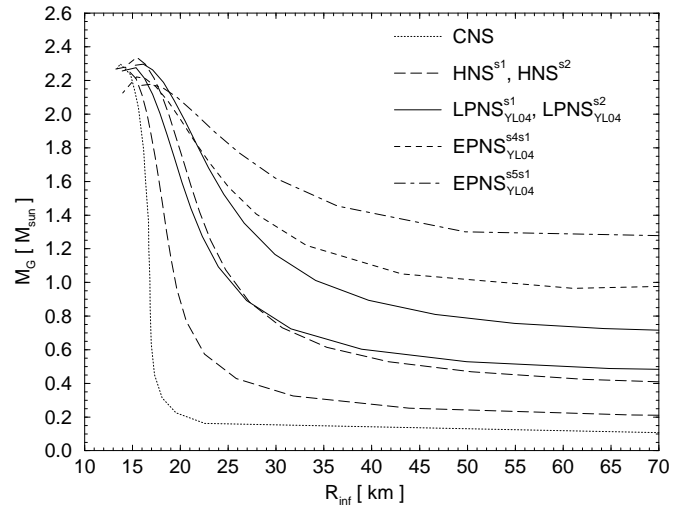


Fig. 14. The gravitational mass versus equatorial radius (as measured by an observer located at infinity) of NS's and PNS's rotating at their Kepler frequency. The lower long dashed line corresponds to the HNS^{s1} EOS and the upper long dashed line to the HNS^{s2} EOS. The lower solid line corresponds to the $\text{LPNS}_{\text{YL04}}^{\text{s1}}$ EOS and the upper solid line to the $\text{LPNS}_{\text{YL04}}^{\text{s2}}$ EOS.

at fixed central energy density, but the maximum mass is reached for lower central energy densities (see also Table 5). The mass increase due to rotation is smaller for PNS's than for CNS's, since the radii of PNS's are larger and thus the Kepler frequencies are smaller.

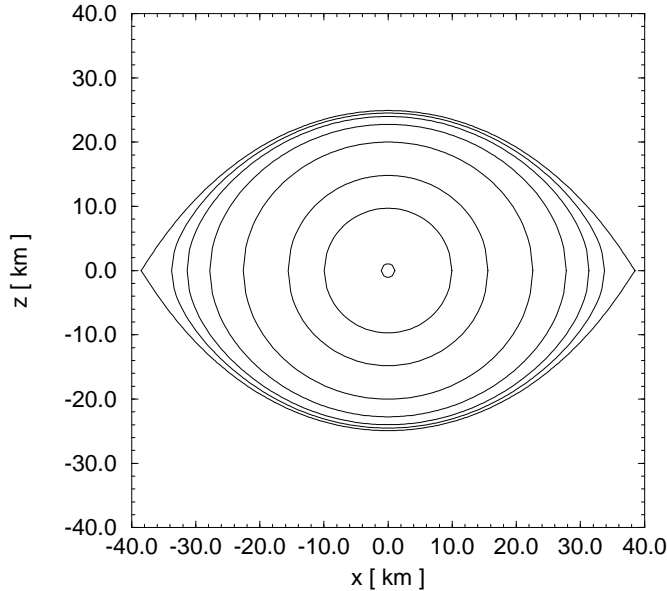


Fig. 15. Iso-energy-density surfaces for a EPNS^{s5s1}_{YL04} model with a baryonic mass of $1.5M_{\odot}$ rotating at its Kepler frequency. The surfaces correspond to energy-densities (beginning at the centre), $\varepsilon = 0.99, 0.1, 0.01, 10^{-3}, 10^{-4}, 10^{-5}, 10^{-6}\varepsilon_c$, where $\varepsilon_c = 8.07 \times 10^{14} \text{ g cm}^{-3}$ denotes the central energy-density.

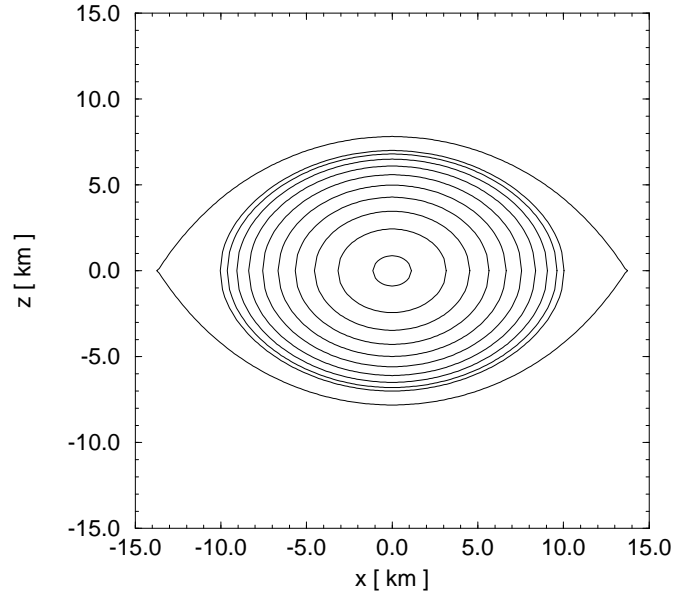


Fig. 16. Iso-energy-density surfaces for a CNS model with a baryonic mass of $1.5M_{\odot}$ rotating at its Kepler frequency. The surfaces correspond to energy-densities (beginning at the centre), $\varepsilon = 0.99, 0.9, 0.8, 0.7, 0.6, 0.5, 0.4, 0.3, 0.2, 0.1\varepsilon_c$, where $\varepsilon_c = 8.11 \times 10^{14} \text{ g cm}^{-3}$ denotes the central energy-density.

We also show the mass-radius relation for PNS's in Figs. 13 and 14⁸. In comparison with CNS's, where the radius only slightly changes in the relevant mass region around $M_G \sim 1.4M_{\odot}$, one obtains for PNS's a much stronger increase of the radius with decreasing mass, which is caused by the stiffer EOS's for the PNS's.

To demonstrate the differences of the internal structure of an EPNS and a CNS, we show in Figs. 15 and 16 the iso-energy-density surfaces for models with $M_B = 1.5M_{\odot}$. It turns out that EPNS's contain mainly matter of densities below nuclear matter density (Fig. 15). Contrary to this, matter in a CNS is dominated by matter of densities around and above nuclear matter density (Fig. 16).

Another important point concerns the stability of the star models against secular or dynamical instabilities. A certain configuration is dynamically stable against axisymmetric perturbations if the gravitational mass is minimum with respect to variations at fixed baryon number and angular momentum. Along a star sequence with fixed angular momentum, this is the case if the gravitational mass increases with the central energy density (see Shapiro & Teukolsky 1983, p. 151). Please note that the angular momentum is not fixed in the sequences of stars rotating with Kepler frequency. The maximum mass configuration differs therefore slightly from the marginally stable configuration. A fully general relativistic analysis of dynamical and secular stability against non-axisymmetric

perturbations is extremely difficult and has been performed only by means of approximations and/or special assumptions in literature. It turned out however that the configurations can be classified by a stability parameter defined by the ratio of the kinetical energy and the absolute value of the gravitational energy, $\beta = E_{\text{kin}}/|E_{\text{grav}}|$. For values, $\beta \gtrsim 0.26$, the models are probably dynamically unstable against the bar mode ($m = 2$), whereas they become already secularly unstable for $\beta \gtrsim 0.14$ (see, e.g., Durisen 1975; Managan 1985; Imamura et al. 1985; Bonazzola et al. 1996). Higher modes, $m \gtrsim 5$, of perturbations are suppressed by the finite viscosity of neutron star matter. It is however uncertain whether modes with $m = 3$ or 4 are also suppressed. If this is not the case, secular instability sets already in above a critical value, $\beta \gtrsim 0.08$ (Friedman et al. 1986).

Figure 17 shows the value of the stability parameter for stars rotating with their Kepler frequency. Since the timescale for the growing of the secular instabilities is larger than the evolution timescale of PNS's and HNS's, only the dynamical instability is important for PNS's and HNS's. The critical value for the dynamical instability, $\beta \gtrsim 0.26$, is reached by none of the models. Depending on the internal structure of the CNS's, the CNS's models rotating with Kepler frequency may become secular unstable against modes with $m = 3$ or $m = 4$ for star masses $M \gtrsim 0.8M_{\odot}$.

⁸ The equatorial radius R_{inf} is the circumferential radius as measured in infinity (see, e.g., Schaab 1998)

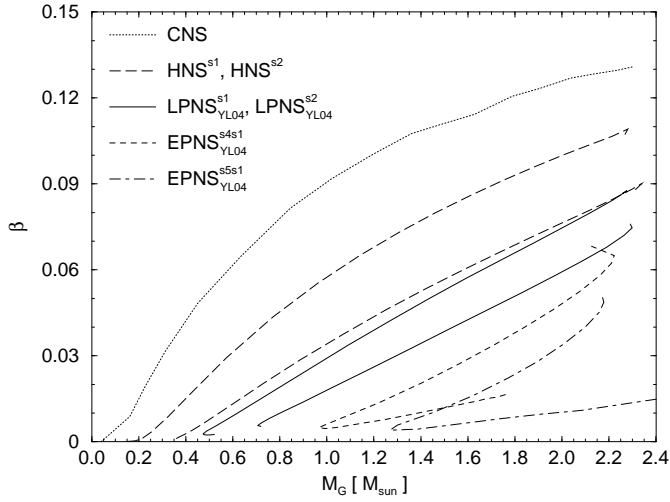


Fig. 17. Stability parameter $\beta = E_{\text{kin}}/|E_{\text{grav}}|$ versus gravitational mass of PNS's and NS's rotating at their Kepler frequency for different EOS's. The upper long dashed line corresponds to the HNS^{s1} EOS and the lower long dashed line to the HNS^{s2} EOS. The upper solid line corresponds to the $\text{LPNS}^{s1}_{\text{YL04}}$ EOS and the lower solid line to the $\text{LPNS}^{s2}_{\text{YL04}}$ EOS.

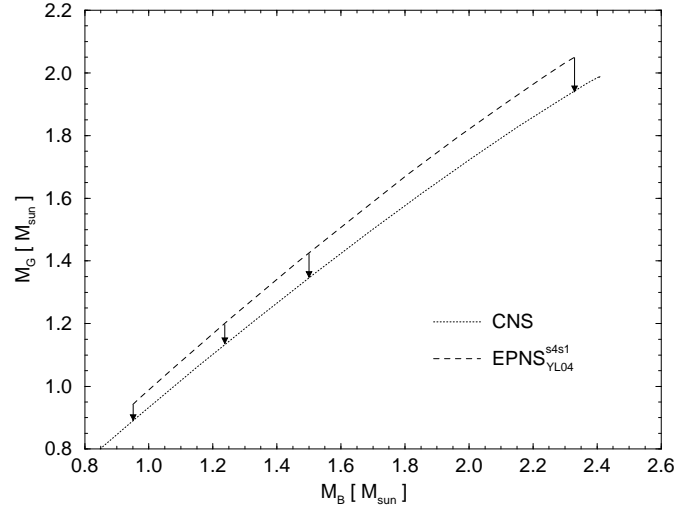


Fig. 18. Gravitational mass versus baryonic mass for the non-rotating $\text{EPNS}^{s4s1}_{\text{YL04}}$ EOS and the non-rotating CNS EOS. The $\text{EPNS}^{s5s1}_{\text{YL04}}$ EOS lies exactly on the $\text{EPNS}^{s4s1}_{\text{YL04}}$ line and is not shown by that reason. The arrows show the evolution (from left to right) for the minimum mass $\text{EPNS}^{s4s1}_{\text{YL04}}$, the minimum mass $\text{EPNS}^{s5s1}_{\text{YL04}}$, the $M_B = 1.5 M_\odot$, and the maximum mass configurations.

4.2. Evolution of a non-rotating protoneutron star

The evolution of a PNS to a CNS can be followed by means of several “snapshots” taken at different times after core bounce (see Sect. 2). The evolution path is determined by fixing the baryonic mass and the angular momentum if accretion of matter and loss of angular momentum is neglected. First, we study the evolution of a non-rotating PNS with $M_B = 1.5 M_\odot$ (see Table 3 and Fig. 18).

The first snapshot corresponds to approximately 50 - 100 ms when the envelope is characterized by a high entropy per baryon and high lepton number (see curves labeled $\text{EPNS}^{s5s1}_{\text{YL04}}$ and $\text{EPNS}^{s4s1}_{\text{YL04}}$). After 0.5 - 1 seconds the PNS reached our LPNS stage, which is characterized by an approximately constant entropy per baryon, $s \sim 2$, throughout the star (model $\text{LPNS}^{s2}_{\text{YL04}}$). Due to the higher entropy per baryon in the core of the PNS, the central density and thus the gravitational binding energy decreases. On the other hand the entropy per baryon decreases in the envelope and therefore the radius decreases, too. For a lower value of the entropy per baryon and/or a lower value for the lepton number, the gravitational binding energy increases compared to the EPNS stage (models $\text{LPNS}^{s1}_{\text{YL03}}$, $\text{LPNS}^{s1}_{\text{YL04}}$, $\text{LPNS}^{s1}_{\text{YL03}}$). After about 10 - 30 seconds the neutrinos escape from the star and its EOS softens (HNS models). The gravitational binding energy thus increases by roughly 3 %. Finally, the CNS model is even more compressed.

Due to a smaller increase of the pressure with increasing temperature, Burrows & Lattimer (1986) and Pons et al. (1999) obtain a monotonous increase of the cen-

tral density during the evolution of the PNS to the CNS. In contrast, our results, and also those of Keil & Janka (1995), show a more complex behaviour of the central density (see discussion in the paper of Pons et al. 1999). This difference has mainly two reasons: Firstly, Pons et al. (1999) use an entropy profile obtained in a supernova collapse simulation of a $1.08 M_\odot$ NS, which leads to a higher central entropy per baryon, $s \sim 1.5$, at the EPNS stage and an increase to $s \sim 2$ at the LPNS stage. We use the calculations of Burrows et al. (1995) who simulated the supernova collapse of a NS with $M \sim 1.5 M_\odot$. They obtained a smaller starting central entropy per baryon, $s \sim 1$, and an increase to $s \sim 2$ at the LPNS stage. The second reason is the fact, that they use an approximation for the temperature influence on the pressure (derived by Prakash et al. 1997) of the nucleons:

$$s = \frac{\pi^2}{2} T \sum_{\tau=n,p} \frac{Y_\tau}{T_{F,\tau}}, \quad (11)$$

$$\frac{P_{\text{th}}}{P_0} = \frac{5s}{3\pi^2} \frac{\sum_\tau \frac{Y_\tau}{T_{F,\tau}} \left(1 - \frac{3}{2} \frac{d \ln m_\tau^*}{d \ln n_\tau}\right)}{\left(\sum_\tau \frac{Y_\tau}{T_{F,\tau}}\right)^2 (\sum_\tau Y_\tau T_{F,\tau})} \left(1 + \frac{P_{\text{pot}}}{P_{\text{kin}}}\right)^{-1}, \quad (12)$$

where $T_{F,\tau}$ denotes the Fermi temperature of the quasi particles ($T_{F,\tau} = p_{F,\tau}^2/2m_\tau^*$), P_{th} , the thermal pressure and $P_0 = P_{\text{kin}} + P_{\text{pot}}$, the pressure at zero temperature as sum of kinetic and potential pressure. This approximation holds under the assumption that in the dense

Table 3. Properties of non-rotating and with Kepler frequency rotating PNS's and NS's, for a fixed baryonic mass $M_B = 1.5 M_\odot$. The EOS's are summarized in Table 1. The entries are: gravitational mass, M_G ; baryonic mass, M_B ; circumferential radius (as measured in infinity), R_{inf} ; central baryon number density, n_c ; central temperature, T_c ; Kepler frequency, Ω_K ; angular momentum, J ($M_\odot \text{ km} \hat{=} 5.966 \times 10^{48} \text{ g cm}^2 \text{ s}^{-1}$).

EOS	$\Omega = 0$				$\Omega = \Omega_K$				
	M_G [M_\odot]	R_{inf} [km]	n_c [fm^{-3}]	T_c [MeV]	M_G [M_\odot]	R_{inf} [km]	n_c [fm^{-3}]	Ω_K [s^{-1}]	J [$M_\odot \text{ km}$]
EPNS ^{s5s1} _{YL04}	1.425	25.66	0.440	20.8	1.430	38.55	0.427	1879	0.634
EPNS ^{s4s1} _{YL04}	1.425	18.66	0.456	21.3	1.433	27.46	0.436	3056	0.924
LPNS ^{s2} _{YL04}	1.431	17.38	0.385	39.5	1.437	25.62	0.353	3410	1.234
LPNS ^{T06s2} _{YL04}	1.432	17.47	0.386	39.6	1.437	25.77	0.355	3381	1.219
LPNS ^{s2} _{YL04(64–63)}	1.430	16.72	0.386	39.6	1.438	24.68	0.348	3610	1.340
LPNS ^{s2} _{YL04(64–22)}	1.430	16.34	0.386	39.6	1.438	24.13	0.344	3739	1.408
LPNS ^{s2} _{YL04(64–62)}	1.430	15.85	0.388	39.7	1.439	23.36	0.341	3930	1.497
LPNS ^{s2} _{YL03}	1.414	16.01	0.400	42.9	1.423	23.37	0.361	3897	1.362
LPNS ^{s1} _{YL04}	1.411	14.70	0.459	21.4	1.423	21.26	0.417	4482	1.389
LPNS ^{s1} _{YL03}	1.391	13.59	0.475	22.8	1.406	19.55	0.424	5076	1.552
LPNS ^{s0} _{YL04}	1.410	12.39	0.519	0	1.429	17.73	0.450	5949	1.800
HNS ^{s2}	1.391	15.22	0.412	49.7	1.403	22.13	0.367	4204	1.431
HNS ^{T06s2}	1.392	15.29	0.412	49.7	1.404	22.24	0.369	4171	1.413
HNS ^{T0s2}	1.385	13.53	0.404	49.0	1.407	19.86	0.324	5075	2.072
HNS ^{s1}	1.362	12.78	0.501	26.8	1.382	18.36	0.437	5562	1.669
HNS ^{T03s1}	1.363	12.80	0.502	26.9	1.382	18.39	0.438	5550	1.662
HNS ^{T0s1}	1.362	12.18	0.504	27.0	1.387	17.59	0.418	6023	1.957
CNS	1.346	11.45	0.551	0	1.374	16.36	0.459	6689	1.953

parts of the PNS the temperature is small in comparison with the Fermi temperature, i.e. $T/T_F \ll 1$. However in our case these ratio reaches $T/T_F \approx 0.45$ ($T/T_F \approx 0.6$) at $n = n_0$ and $T/T_F \approx 0.29$ ($T/T_F \approx 0.44$) at $n = 1 \text{ fm}^{-3}$ for neutrons (protons) in the LPNS^{s2}_{YL04} model (see also the Fermi-Dirac distribution function in Fig. A.1 of Appendix A and Takatsuka et al. (1994) for this purpose, in which it can be seen that more than 10 % of the matter is non-degenerate). Therefore this approximation underestimates the pressure increase due to thermal effects, e.g. the thermal pressure P_{th} is exact (approximative) 2.37 MeVfm^{-3} (1.26 MeVfm^{-3}) at $n = n_0$ and 54.62 MeVfm^{-3} (28.83 MeVfm^{-3}) at $n = 1 \text{ fm}^{-3}$ for the nucleons of the LPNS^{s2}_{YL04} case of our model. Hence in our opinion, higher order terms should be included in the treatment. Since the temperature dependence of the GM3 model of Pons et al. (1999) is smaller than in our case, the deviations between the exact solution and the approximation may be small.

4.3. Maximum rotational frequency of a neutron star

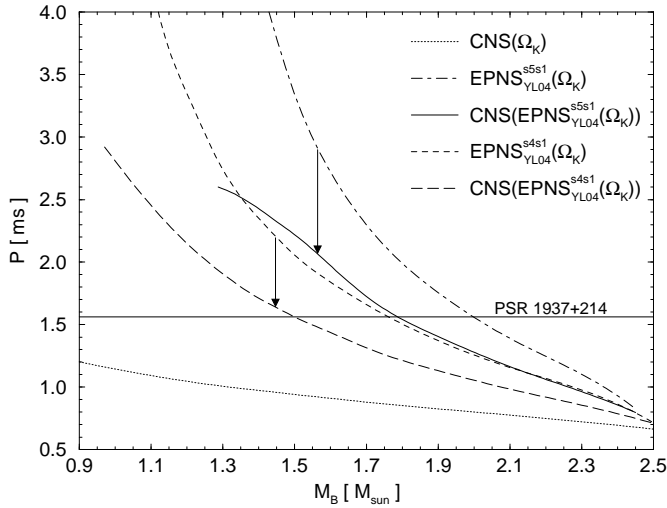
We follow now the evolution of an EPNS with $M_B = 1.5 M_\odot$, which rotates with Kepler frequency at its EPNS

state. During its evolution, the angular momentum is assumed to be conserved (see Table 4). As in the non-rotating case, the star becomes more and more compressed during its evolution. With only a few exceptions, the central baryon density increases, whereas the gravitational mass and the circumferential radius decreases. It is obvious that this trend has to be counterbalanced by an increasing angular velocity in order to keep the angular momentum constant. Compared to the EPNS state, the angular velocity in the CNS state is increased by 51 % or 32 % for the sequences starting with the model EPNS^{s5s1}_{YL04} or EPNS^{s4s1}_{YL04}, respectively. Nevertheless, the angular velocity in the CNS state reaches at most 60 % of the Kepler frequency.

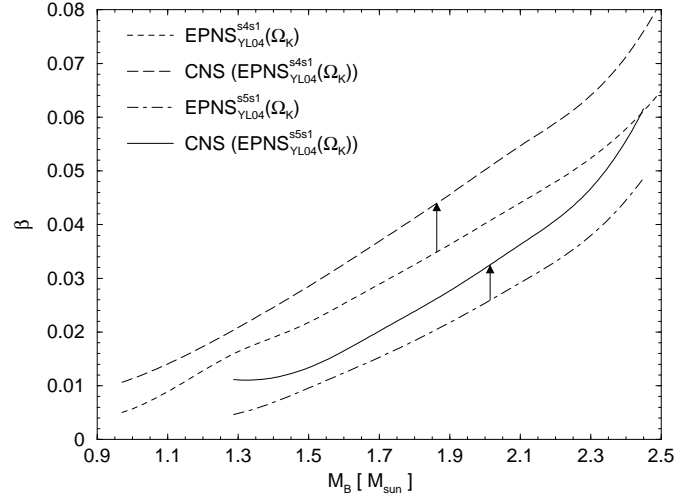
In this respect, the minimum rotational period is determined by the Kepler rotating EPNS model. Figure 19 shows the the general evolution of the rotational period for the two EPNS models. For a CNS with a typical baryonic mass of $1.5 M_\odot$ one obtains a minimum rotational period, P , between 1.56 and 2.22 ms. Recently, Goussard et al. (1997, 1998) found similar results for the minimum rotational period, which confirms our calculations. The period of the fastest known pulsar PSR 1937+214, $P = 1.56 \text{ ms}$ (Backer et al. 1982) is at the lower limit of this range. Pul-

Table 4. Evolution of $1.5 M_\odot$ star at constant angular momentum, $J = 0.634 M_\odot \text{ km}$ and $J = 0.924 M_\odot \text{ km}$ for the sequences starting with the model EPNS_{YL04}^{s5s1} and EPNS_{YL04}^{s4s1}, respectively.

EOS	EPNS _{YL04} ^{s5s1}					EPNS _{YL04} ^{s4s1}				
	M_G [M_\odot]	R_{inf} [km]	n_c [fm ⁻³]	T_c [MeV]	Ω [s ⁻¹]	M_G [M_\odot]	R_{inf} [km]	n_c [fm ⁻³]	T_c [MeV]	Ω [s ⁻¹]
EPNS	1.430	38.55	0.427	20.4	1879	1.433	27.46	0.436	20.7	3056
LPNS _{YL04} ^{s2}	1.349	14.83	0.350	37.0	2091	1.341	15.40	0.336	36.0	2961
LPNS _{YL03} ^{s2}	1.363	14.27	0.374	40.9	2171	1.361	14.74	0.362	39.9	3073
LPNS _{YL04} ^{s1}	1.391	13.17	0.442	20.9	2377	1.391	13.54	0.430	20.5	3390
LPNS _{YL03} ^{s1}	1.385	12.76	0.462	22.4	2474	1.387	13.09	0.451	22.0	3525
HNS _{YL03} ^{s2}	1.349	14.06	0.387	46.5	2246	1.348	14.53	0.375	46.3	3178
HNS _{YL03} ^{s1}	1.362	12.49	0.489	26.3	2609	1.365	12.83	0.478	25.9	3709
CNS	1.348	11.83	0.535	0	2833	1.351	12.14	0.523	0	4031

**Fig. 19.** Minimum rotational period P versus baryonic mass of the EPNS's and CNS's. The figure shows the spin up during the evolution of the EPNS's to CNS's. The dot-dashed (short dashed) line shows the EPNS_{YL04}^{s5s1} (EPNS_{YL04}^{s4s1}) model rotating at its Kepler frequency. The solid (long dashed) line shows the corresponding CNS model obtained by cooling at constant angular momentum. The dotted line shows CNS's rotating at their Kepler frequency for comparison. The arrows represent the evolution from the EPNS stage to the CNS stage.

sars that rotate even faster cannot be born with such small periods but have to be accelerated after their formation, as long as a typical baryonic mass, $M_B = 1.5 M_\odot$ is assumed. Andersson (1998) has recently shown that not too cold NS's rotating with $\Omega \gtrsim 0.1 \Omega_K$ are unstable against r-modes. This means that the minimum rotational period for a young NS is even higher, $P_{\text{min}} \sim 10$ ms. Both the results by Andersson (1998) and the results presented here

**Fig. 20.** Variation of the stability parameter $\beta = E_{\text{kin}}/|E_{\text{grav}}|$ during the evolution from EPNS's to CNS's at constant angular momentum. The arrows represent the evolution from the EPNS stage to the CNS stage.

strengthen the view of millisecond pulsars as being recycled by accretion (Lorimer 1996).

Figure 20 shows the behaviour of β during the evolution from the EPNS to the CNS state. The stability parameter increases during the evolution. Nevertheless, its maximum value, $\beta \sim 0.082$, reached for the most massive star of the EPNS_{YL04}^{s4s1} EOS, is only a little larger than the critical value $\beta \sim 0.08$ for the onset of the secular instabilities with $m = 3, 4$ (see Sect. 4.1).

4.4. Maximum and minimum mass of a neutron star

Table 5 shows, that the maximum baryonic mass of a non-rotating (rotating) EPNS is $2.33 M_\odot$ ($2.45 - 2.5 M_\odot$),

Table 5. Properties of the maximum gravitational mass configurations of non-rotating and with Kepler frequency rotating PNS's and NS's.

EOS	$\Omega = 0$					$\Omega = \Omega_K$					
	M_G [M_\odot]	M_B [M_\odot]	R_{inf} [km]	n_c [fm $^{-3}$]	T_c [MeV]	M_G [M_\odot]	M_B [M_\odot]	R_{inf} [km]	n_c [fm $^{-3}$]	Ω_K [s $^{-1}$]	J [M_\odot km]
EPNS $^{s5s1}_{\text{YL04}}$	2.05	2.33	12.59	1.09	40.4	2.18	2.45	16.93	1.08	7609	3.06
EPNS $^{s4s1}_{\text{YL04}}$	2.05	2.33	11.83	1.10	40.7	2.22	2.50	15.44	1.09	8803	3.69
LPNS $^{s2}_{\text{YL04}}$	2.09	2.33	11.91	1.03	81.6	2.30	2.54	15.90	0.97	8602	4.29
LPNS $^{s2}_{\text{YL03}}$	2.08	2.37	11.29	1.09	92.0	2.33	2.62	15.43	0.95	9067	4.61
LPNS $^{s1}_{\text{YL04}}$	2.05	2.33	10.82	1.14	41.8	2.28	2.56	15.38	0.93	9384	4.49
LPNS $^{s1}_{\text{YL03}}$	2.04	2.38	10.70	1.18	45.6	2.31	2.65	14.43	0.93	9701	4.94
LPNS $^{s0}_{\text{YL04}}$	2.05	2.27	10.29	1.12	0	2.28	2.54	14.31	0.88	9956	4.98
HNS s2	2.08	2.41	11.24	1.12	120.6	2.34	2.68	15.47	0.92	9073	4.80
HNS s1	2.01	2.38	10.48	1.20	62.1	2.28	2.66	14.14	0.92	9864	5.03
CNS	1.99	2.41	9.83	1.25	0	2.30	2.70	13.74	0.95	10631	5.64

whereas the maximum baryonic mass of a CNS is $2.41 M_\odot$ ($2.7 M_\odot$) (see also Fig. 18). Since the maximum baryonic mass of a LPNS and HNS is larger than the maximum baryonic mass of a EPNS, too, it is obvious that a PNS based on our nuclear EOS cannot collapse to a black hole during its Kelvin-Helmholtz cooling phase if any further accretion is neglected (see Baumgarte et al. 1996). The situation changes if hyperons, meson condensation, or a quark-hadron phase transition are included (see, e.g., Brown & Bethe 1994; Pandharipande et al. 1995; Prakash et al. 1995; Glendenning 1995). Another important point concerning the maximum mass of a CNS is due to the different maximum masses of EPNS's and CNS's rotating at their Kepler frequencies. The EPNS can support a baryonic mass of $2.45 - 2.5 M_\odot$, which is only slightly higher than the maximum baryonic mass of the non-rotating CNS ($2.41 M_\odot$), but $0.2 - 0.25 M_\odot$ less than the maximum baryonic mass of the CNS rotating at its Kepler frequency. Such supramassive CNS's enter unstable regions during their spin down evolution due to instability against axisymmetric perturbations and may finally collapse to a black hole. For a discussion of these supramassive CNS's, see Cook et al. (1994) and Salgado et al. (1994).

In first approximation, the gravitational mass of non-rotating PNS's and HNS's increases quadratically with the entropy per baryon, which is taken constant throughout the star (see Prakash et al. 1997):

$$M_G(s) = M_G(T=0) (1 + \lambda s^2 + \dots). \quad (13)$$

We obtain for λ approximate values $\sim 0.010 - 0.011$ (~ 0.005) for the cases without (with) trapped lepton number (see Table 5). These values are in agreement with the values derived by Prakash et al. (1997). In the investigation of Goussard et al. (1997) the gravitational mass

shows the opposite behaviour: The gravitational mass decreases slightly with increasing entropy per baryon. This is probably caused by the smaller temperature dependence of the EOS of Lattimer & Swesty (1991), as it was pointed out in Sect. 3. In the case of rotating stars the behaviour seems to be more complex since the value of λ is negative for HNS s1 and LPNS $^{s1}_{\text{YL04}}$ and positive for HNS s2 and LPNS $^{s2}_{\text{YL04}}$. Another interesting point is, that the maximum gravitational and baryonic mass of the non-rotating PNS's are determined by the EOS used in the core and do not depend on the EOS used in the envelope (compare the models EPNS $^{s4s1}_{\text{YL04}}$, EPNS $^{s5s1}_{\text{YL04}}$, and LPNS $^{s1}_{\text{YL04}}$ in Table 5 and Figs. 10 and 13). In the case of rotating PNS's, the maximum gravitational mass of the EPNS is however smaller compared to the corresponding LPNS model (see Table 5 and Figs. 12 and 14). This behaviour is caused by the higher Kepler frequency which can be supported by the LPNS models (see Sect. 4.1).

The minimum baryonic mass of our non-rotating EPNS sequences is in the range $0.95 - 1.24 M_\odot$. The minimum mass is increased in the case of Kepler rotating stars to $0.97 - 1.29 M_\odot$. If accretion is neglected the baryonic mass is conserved during the evolution of the EPNS to the CNS. We follow the evolution of the minimum mass EPNS $^{s5s1}_{\text{YL04}}$ and EPNS $^{s4s1}_{\text{YL04}}$ model to a CNS via the LPNS and the HNS stage (see Table 6). The minimum mass of a CNS born in a supernova is therefore determined by the minimum mass model of the EPNS sequence. The above ranges of baryonic mass correspond to a lower limit of the gravitational CNS's mass in the range $0.89 - 1.13 M_\odot$. This is by a factor of ten larger than the minimum mass of the CNS sequence. This property of EPNS's was also recently found by Goussard et al. (1998).

Table 6. Evolution of minimum mass star for the non-rotating EPNS_{YL04}^{s5s1} EOS ($M_B = 1.238M_\odot$) and the EPNS_{YL04}^{s4s1} EOS ($M_B = 0.950M_\odot$).

EOS	EPNS _{YL04} ^{s5s1}				EPNS _{YL04} ^{s4s1}			
	M_G [M_\odot]	R_{inf} [km]	n_c [fm ⁻³]	T_c [MeV]	M_G [M_\odot]	R_{inf} [km]	n_c [fm ⁻³]	T_c [MeV]
EPNS	1.207	45.61	0.340	17.3	0.942	44.49	0.281	15.1
LPNS _{YL04} ^{s2}	1.199	19.77	0.308	33.8	0.926	25.34	0.219	26.7
LPNS _{YL03} ^{s2}	1.186	17.49	0.327	37.1	0.922	20.38	0.250	30.7
LPNS _{YL04} ^{s1}	1.185	15.83	0.384	18.9	0.926	18.05	0.307	16.1
LPNS _{YL03} ^{s1}	1.168	14.24	0.404	20.3	0.915	15.31	0.331	17.6
HNS ^{s2}	1.168	16.28	0.341	43.2	0.911	18.26	0.267	36.5
HNS ^{s1}	1.146	13.18	0.429	23.7	0.898	13.75	0.354	20.5
CNS	1.134	11.53	0.481	0	0.890	11.58	0.410	0

Variations of the location of the transition region between the envelope (high entropy per baryon) and the core (low entropy per baryon) of the EPNS's do not change the minimum mass considerably. Starting the transition region at lower densities will lead to smaller minimum masses of the EPNS's, but the lower the initial mass of the EPNS is, the higher is the entropy per baryon in the envelope and in the core (see e.g. Keil et al. 1996; Pons et al. 1999). This effect drives the minimum mass back to higher values, so that our results of the minimum mass range is a good approximation (see also Goussard et al. 1998).

Timmes et al. (1996) examine the most likely masses of NS's using the numerical data of Woosley & Weaver (1995) who simulated Type-II supernovae with progenitor stars in the mass range between 11 and 40 M_\odot . They obtain a lower limit of the NS mass, which depends on the mass and the composition of the progenitor, of 1.15 – 1.27 M_\odot . This lower limit is comparable to our results.

4.5. Sensitivity of the results

In Table 3, we compare the properties of our PNS and NS models for a fixed baryonic mass, $M_B = 1.5 M_\odot$. This canonical value corresponds to the measured gravitational masses, $1.35 \pm 0.27 M_\odot$, of neutron stars in binary systems (see Thorsett et al. 1993; Van Kerkwijk et al. 1995).

As can be inferred by comparing the LPNS models LPNS_{YL04(64–62)}^{s2}, LPNS_{YL04(64–22)}^{s2}, and LPNS_{YL04(64–63)}^{s2} with the model LPNS_{YL04}^{s2} (see Sect. 2.2), the location of the neutrino sphere has nearly no effect on the gravitational mass and the central density. However, the circumferential radius and the Kepler frequency vary by up to 10 % and 15 %, respectively.

The use of an isothermal, instead of an isentropic, EOS in the envelope of the HNS models HNS^{T03s1} and HNS^{T06s2} has only small effects on the properties of the HNS's (see Table 3). If thermal effects in the envelope are however neglected (models HNS^{T0s1} and HNS^{T0s2}), the circumferential radius is reduced by $\sim 10\%$. This yields to an increase of the Kepler frequency by $\sim 20\%$. Though the assumption of zero temperature in the envelope does not change the resulting mass and central densities, the error made in the circumferential radius and in the Kepler frequency might be rather large.

5. Discussion and conclusion

The aim of this paper was the investigation of the properties of rapidly rotating PNS's consisting of nuclear matter (n, p, e⁻, μ^-) under the influence of trapped neutrinos. We used a recently developed nuclear EOS for hot, dense matter in the nuclear Thomas-Fermi approach (Strobel et al. 1999). The nuclear EOS was extended in this paper to subnuclear densities and to different compositions of PNS and HNS matter (i.e. trapped neutrinos, constant entropy per baryon, ...). Our results for subnuclear densities are comparable to the results derived by Lattimer & Swesty (1991) used in the investigations of Goussard et al. (1997, 1998) and Gondek et al. (1997). However, considerable deviations occur at densities around and above nuclear matter density, since the EOS of Lattimer & Swesty (1991) shows a smaller temperature dependence. In general, this difference to our results has only a small impact on the properties of PNS's, but impacts on HNS's with canonical mass. The impact becomes considerable for more massive stars.

An investigation of this kind should investigate the properties of PNS's and HNS's for the whole range of possible masses. So far lepton concentration profiles and en-

entropy per baryon profiles were derived only for one fixed mass in simulations of PNS evolution (e.g. Burrows & Lattimer 1986; Keil & Janka 1995; Burrows et al. 1995). In our calculation, the extension to the whole range of masses was done by assuming that the lepton concentration and the entropy per baryon does not depend on the mass of the PNS.

As a result we find that the minimum gravitational mass of a NS is determined at the earliest stage of a PNS, so that the mass of a NS formed in a Type-II supernova is larger than $0.89 - 1.13 M_{\odot}$, which confirms similar results of a recent investigation by Goussard et al. (1998). The exact lower limit of the NS mass depends on the used entropy per baryon in the EPNS model. The quoted mass range was obtained by using $s = 4$ and $s = 5$ as lower and upper limit of the entropy per baryon in the envelope of the EPNS (Burrows et al. 1995). The minimum mass of EPNS's is approximately by a factor of ten larger than the minimum stable mass of CNS's.

The maximum possible baryonic mass of a CNS is always larger than the maximum possible baryonic mass of the PNS's, this means that once a PNS was formed, it cannot collapse into a black hole, if further accretion is neglected (see also Takatsuka 1995; Bombaci 1996). One exception is the case of the most massive stars rotating near or at its Kepler frequency, which possibly collapse to a black hole during their time evolution, for a discussion, see Cook et al. (1994) and Salgado et al. (1994). This statement holds for stars with a pure nucleonic/leptonic composition. If one includes hyperons and/or quarks, the maximum baryonic mass of a CNS decreases (e.g. Huber et al. 1998; Balberg et al. 1999) and may be smaller than the maximum baryonic mass of a PNS. Then, a sufficiently massive PNS may collapse to a black hole during deleptonization (Prakash et al. 1997). The maximum gravitational mass increases slightly with increasing entropy per baryon in contrast to the maximum baryonic mass (see also Prakash et al. 1997). As it was pointed out, Goussard et al. (1997) got a different result due to the use of the EOS derived by Lattimer & Swesty (1991).

It turned out that the influence of rotation has several impacts on properties of PNS's and NS's. Whereas the minimum mass changes only slightly due to rotation, the effect on the maximum mass is rather large, particularly for CNS's. The central baryon density is nearly unaffected by rotation at the early stages of the evolution, whereas the impact on the later stages is rather large. The effect on the circumferential radius decreases with increasing mass and the impact on EPNS's and LPNS's is slightly larger than the impact on CNS's.

We investigated the influence of different shapes of the neutrino sphere on the structure of LPNS's. As expected, we obtained considerable differences (up to 10%) in the circumferential radii and, due to this, in the Kepler frequency. Other properties, as the central density, are barely changed by the location of the neutrino sphere. We have

also considered different temperatures in the envelope of LPNS's and HNS's. If a very high temperature of 0.6 MeV is used in the envelope instead of a constant entropy per baryon, the gross properties of the LPNS change by less than 1%. Larger deviations were obtained if the envelope is assumed to be cold. The finite temperature effects should therefore not be neglected in the envelope. Furthermore, we obtain that the thermal effects are comparable to the effects due to trapped neutrinos. This is in contrast to the results of Prakash et al. (1997), who found the thermal effects to be much smaller than the effect of high lepton numbers.

In our model we assumed that accretion onto the emerging NS stopped after the formation of the EPNS (see Burrows et al. 1995). Furthermore, we kept the angular momentum constant during the deleptonization and the thermal cooling period. Under these presumptions, we obtain a lower limit on the periods of young NS's with a typical baryonic mass of $1.5 M_{\odot}$ between 1.56 and 2.22 ms, which is in accordance with similar values obtained by Goussard et al. (1997, 1998). These results support strongly the hypothesis that millisecond pulsars were accelerated due to accretion. With the same reasoning, one obtains an upper limit of the stability parameter $\beta \lesssim 0.082$, which is smaller, for almost all NS's, than the critical value for the onset of dynamical and secular instabilities. Kepler rotating massive CNS's possess stability parameter values up to $\beta \sim 0.13$ and might therefore be secular unstable against $m = 2$ and $m = 3$ non-axisymmetric perturbations.

Though we have assumed uniform rotation, it seems to be very reasonable that PNS's and young NS's rotate differentially (e.g. Janka & Mönchmeyer 1989). As it was found by Schaab (1998) and Goussard et al. (1998), differential rotation may considerably effect the structure of PNS's and NS's, and we will pursue our investigations to differential rotation in the future. Another issue that will be addressed in a future work is the effect of additional degrees of freedom (e.g. hyperons) on the evolution of PNS's.

Acknowledgements. We want to thank Wolfgang Keil, Georg Raffelt, Thomas Strobel and Fridolin Weber for many helpful discussions. Two of us, K. S. and Ch. S., gratefully acknowledge the Bavarian State for financial support.

Appendix A: Nuclear equation of state

The momentum and density dependent interaction is given by [the upper (lower) sign corresponds to nucleons with equal (unequal) isospin] (Myers & Świątecki 1990):

$$v_{12\tau} = -\frac{2T_{0\tau}}{n_0} g(r_{12}) \left(\frac{1}{2}(1 \mp \xi)\alpha - \frac{1}{2}(1 \mp \zeta) \left(\beta \left(\frac{p_{12}}{p_0} \right)^2 - \gamma \frac{p_0}{|p_{12}|} + \sigma \left(\frac{2\bar{n}}{n_0} \right)^{\frac{2}{3}} \right) \right). \quad (\text{A.1})$$

The quantities n_0 , p_0 , and $T_{0\tau}$ ($= p_0^2/2m_\tau$) [$T_0 = p_0^2/2\bar{m}$ with $\bar{m} = 0.5(m_n + m_p)$, see (A.4)] denote the baryon number density, Fermi momentum, and the kinetic single-particle energy of symmetric nuclear matter at saturation (τ denotes the isospin), respectively. The choice $\xi \neq \zeta$ leads to a better description of asymmetric nuclear systems, and the behaviour of the optical potentials is improved by the term $\sigma(2\bar{n}/n_0)^{2/3}$, where $\bar{n}^{2/3} = 0.5(n_1^{2/3} + n_2^{2/3})$.

The parameter set is given by the most recent adjustment of Myers & Świątecki (1996, 1998): $\alpha = 1.94684$, $\beta = 0.15311$, $\gamma = 1.13672$, $\sigma = 1.05$, $\xi = 0.27976$, and $\zeta = 0.55665$, which leads to the following properties of symmetric nuclear matter at saturation density ($n_0 = 0.16114 \text{ fm}^{-3}$): energy per baryon $u_0 = -16.24 \text{ MeV}$, incompressibility $K = 234 \text{ MeV}$, symmetry energy $J = 32.65 \text{ MeV}$ and effective nucleon mass $m_\tau^*/m_\tau = 0.867$.

The potentials radial dependence, g , is chosen to be of Yukawa type. The function is normalized to unity:

$$\int_{-\infty}^{+\infty} g(r_{12}) d^3r_1 = 1. \quad (\text{A.2})$$

This leads to the following single particle energy u (Strobel et al. 1999):

$$u = \frac{2}{n(2\pi)^3} \sum_{\tau} \int_{-\infty}^{+\infty} \left(\frac{p_1^2}{2m_\tau} + \frac{1}{2} V_\tau(p_1) \right) f_\tau(p_1) d^3p_1, \quad (\text{A.3})$$

with the one-particle potential $V_\tau(p_1)$:

$$\begin{aligned} V_\tau(p_1) = & -\frac{2}{(2\pi)^3} \frac{2T_{0\tau}}{n_0} \int_{-\infty}^{+\infty} \left(\alpha_1 - \beta_1 \left(\frac{p_{12}}{p_0} \right)^2 + \gamma_1 \frac{p_0}{|p_{12}|} - \sigma_1 \left(\frac{2\bar{n}}{n_0} \right)^{\frac{2}{3}} \right) f_\tau(p_2) d^3p_2 \\ & - \frac{2}{(2\pi)^3} \frac{2T_0}{n_0} \int_{-\infty}^{+\infty} \left(\alpha_u - \beta_u \left(\frac{p_{12}}{p_0} \right)^2 + \gamma_u \frac{p_0}{|p_{12}|} - \sigma_u \left(\frac{2\bar{n}}{n_0} \right)^{\frac{2}{3}} \right) f_{-\tau}(p_2) d^3p_2, \end{aligned} \quad (\text{A.4})$$

[τ and $-\tau$ denote different isospin and the following abbreviations were used: $\alpha_1 = 0.5(1 - \xi)\alpha$, $\beta_1 = 0.5(1 - \zeta)\beta$, $\gamma_1 = 0.5(1 - \zeta)\gamma$, $\sigma_1 = 0.5(1 - \zeta)\sigma$, $\alpha_u = 0.5(1 + \xi)\alpha$, $\beta_u = 0.5(1 + \zeta)\beta$, $\gamma_u = 0.5(1 + \zeta)\gamma$ and $\sigma_u = 0.5(1 + \zeta)\sigma$] and the baryon number density:

$$n = \frac{2}{(2\pi)^3} \sum_{\tau} \int_{-\infty}^{+\infty} f_\tau(p_1) d^3p_1. \quad (\text{A.5})$$

In the Eqs. (A.3), (A.4), and (A.5) $f_\tau(p)$ denotes the Fermi-Dirac distribution function (see Fig. A.1 as an example) of a baryon with isospin τ ($k_B = 1$):

$$f_\tau(p_1) = \left(1 + \exp\left(\frac{1}{T}(\epsilon_\tau(p_1) - \mu'_\tau)\right) \right)^{-1}, \quad (\text{A.6})$$

where ϵ_τ denotes the one-particle energy:

$$\epsilon_\tau(p_1) = \frac{p_1^2}{2m_\tau} + V_\tau(p_1). \quad (\text{A.7})$$

Hint: μ'_τ in Eq. (A.6) is not the chemical potential in normal sense, because of the density dependent part in the interaction, for an explanation see Myers & Świątecki (1990), Appendix A. The chemical potentials of neutrons and protons, μ_τ , can be derived over the thermodynamic derivatives:

$$\mu_\tau = \left(n \left(\frac{\partial}{\partial n_\tau} \right)_{s, n_{-\tau}} + 1 \right) u + m_\tau = \left(n \left(\frac{\partial}{\partial n_\tau} \right)_{T, n_{-\tau}} + 1 \right) f + m_\tau, \quad (\text{A.8})$$

in which f is the free energy per baryon and m_τ the rest-mass of neutrons or protons.

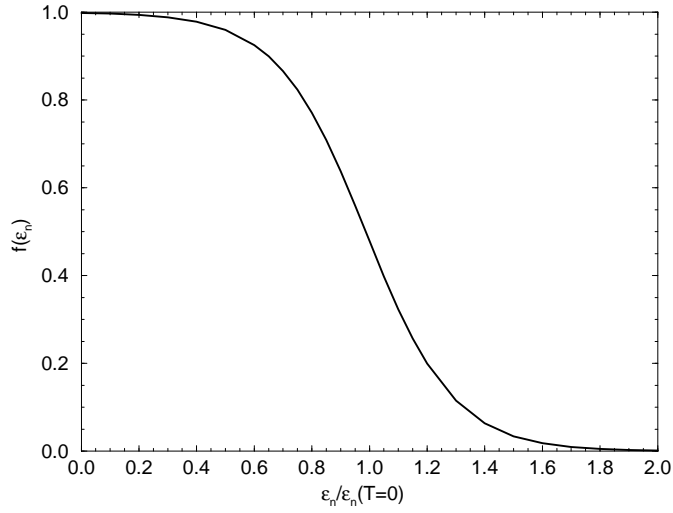


Fig. A.1. Fermi-Dirac distribution function for the neutrons of the LPNS_{YL04}² EOS at $n = 1 \text{ fm}^{-3}$. $T = 79.8 \text{ MeV}$, $T_F = 278.2 \text{ MeV}$, $T/T_F \approx 0.29$, $\mu'_n = 512.8 \text{ MeV}$ and $\epsilon_n(T = 0) = 521.2 \text{ MeV}$ at the Fermi surface.

References

- Andersson N., 1998, *ApJ* 502, 708
- Backer D.C., Kulkarni S.R., Heiles C., Davis M.M., Goss W.M., 1982, *Nat* 300, 615
- Balberg S., Gal A., 1997, *Nucl. Phys. A* 625, 435
- Balberg S., Lichtenstadt I., Cook G.B., 1999, *ApJS* 121, 515
- Bauer M., Hernández-Saldaña E., Hodgson P.E., Quintanilla J., 1982, *J. Phys. G* 8, 525
- Baumgarte T.W., Janka H.-Th., Keil W., Shapiro S.L., Teukolsky S.A., 1996, *ApJ* 468, 823
- Baym G., Pethick C., Sutherland P., 1971, *ApJ* 170, 299
- Bethe H.A., 1990, *Rev. Mod. Phys.* 62, 801
- Bombaci I., 1996, *ApJ* 305, 871
- Bombaci I., Prakash M., Prakash M., et al., 1995, *Nucl. Phys. A* 583, 623
- Bonazzola S., Gourgoulhon E., Salgado M., Marck J.A., 1993, *A&A* 278, 421
- Bonazzola S., Friebe J., Gourgoulhon E., 1996, *ApJ* 460, 379
- Brown G.E., Bethe H.A., 1994, *ApJ* 423, 659
- Burrows A., Lattimer J.M., 1986, *ApJ* 307, 178
- Burrows A., Lattimer J.M., 1988, *Phys. Rep.* 163, 51
- Burrows A., Sawyer R.F., 1998, *Phys. Rev. C* 58, 554
- Burrows A., Hayes J., Fryxell B.A., 1995, *ApJ* 450, 830
- Cook G.B., Shapiro S.L., Teukolsky S.A., 1994, *ApJ* 424, 823
- Cooperstein J., 1988, *Phys. Rep.* 163, 95
- Durisen R.H., 1975, *ApJ* 199, 179
- Friedman J.L., Ipser J.R., Parker L., 1986, *ApJ* 304, 115 + Errata, 1990, *ApJ* 351, 705
- Fukuda Y., Hayakawa T., Ichihara E., et al., 1998, *Phys. Rev. Lett.* 81, 1562
- Glendenning N.K., 1995, *ApJ* 448, 797
- Gondek D., Haensel P., Zdunik J.L., 1997, *A&A* 325, 217
- Goussard J.-O., Haensel P., Zdunik J.L., 1997, *A&A* 321, 822
- Goussard J.-O., Haensel P., Zdunik J.L., 1998, *A&A* 330, 1005
- Haensel P., Salgado M., Bonazzola S., 1995, *A&A* 296, 745
- Hashimoto M.-A., Oyamatsu K., Eriguchi Y., 1994, *ApJ* 436, 257
- Huber H., Weber F., Weigel M.K., Schaab C., 1998, *Int. J. Mod. Phys. E* 7, 301
- Imamura J.N., Friedman J.L., Durisen R.H., 1985, *ApJ* 294, 474
- Janka H.-Th., 1993, in Giovannelli F., Mannocchi G. (eds.), *Proceedings of the Vulcano Workshop, "Frontier Objects in Astrophysics and Particle Physics"*, Vulcano, Italy, May 18-23, 1992, SIF, Bologna, vol. 40, p. 345
- Janka H.-Th., Mönchmeyer R., 1989, *A&A* 226, 69
- Janka H.-Th., Keil W., Raffelt G.G., Seckel D., 1996, *Phys. Rev. Lett.* 76, 2621
- Keil W., 1996, Ph.D. thesis, Technische Universität München, unpublished
- Keil W., Janka H.-Th., 1995, *A&A* 296, 145
- Keil W., Janka H.-Th., Müller E., 1996, *ApJ* 473, L111
- Lattimer J.M., Swesty F.D., 1991, *Nucl. Phys. A* 535, 331
- Lorimer D., 1996, *Physics World* 9, 25
- Managan R.A., 1985, *ApJ* 294, 463
- Mathews G.J., Wilson J.R., Woosley S.E., 1993, in Guidry M.W., Strayer M.R. (eds.), *Proceedings of the First Symposium on "Nuclear Physics in the Universe"*, Oak Ridge, TN, 1992, IOP, Bristol, UK, p. 301
- Mezzacappa A., Calder A.C., Bruenn S.W., et al., 1998, *ApJ* 493, 848
- Myers W.D., Świątecki W.J., 1990, *Ann. Phys. (NY)* 204, 401
- Myers W.D., Świątecki W.J., 1991, *Ann. Phys. (NY)* 211, 292
- Myers W.D., Świątecki W.J., 1995, *Nucl. Phys. A* 587, 92
- Myers W.D., Świątecki W.J., 1996, *Nucl. Phys. A* 601, 141
- Myers W.D., Świątecki W.J., 1998, *Phys. Rev. C* 57, 3020
- Negele J., Vautherin D., 1973, *Nucl. Phys. A* 207, 298
- Pandharipande V.R., 1971, *Nucl. Phys. A* 178, 123
- Pandharipande V.R., Pethick C.J., Thorsson V., 1995, *Phys. Rev. Lett.* 75, 4567
- Pons J.A., Reddy S., Prakash M., Lattimer J.M., Miralles J.A., 1999, *ApJ* 513, 780
- Prakash M., Cooke J.R., Lattimer J.M., 1995, *Phys. Rev. D* 52, 661
- Prakash M., Bombaci I., Prakash M., et al., 1997, *Phys. Rep.* 280, 1
- Raffelt G.G., 1996, *"Stars as Laboratories for Fundamental Physics"*, University of Chicago Press, Chicago
- Raffelt G.G., Strobel T., 1997, *Phys. Rev. D* 55, 523
- Reddy S., Prakash M., Lattimer J.M., 1998, *Phys. Rev. D* 58, 013009

- Romero J.V., Díaz Alonso J., Ibáñez J.M., Miralles J.A., Pérez A., 1992, *ApJ* 395, 612
- Salgado M., Bonazzola S., Gourgoulhon E., Haensel P., 1994, *A&A* 291, 155
- Schaab C., 1998, Ph.D. thesis, Universität München, unpublished
- Schaab C., Weber F., Weigel M.K., Glendenning N.K., 1996, *Nucl. Phys. A* 605, 531
- Schaffner J., Mishustin I.N., 1996, *Phys. Rev. C* 53, 1416
- Shapiro S.L., Teukolsky S.A., 1983, “Black Holes, White Dwarfs and Neutron Stars”, John Wiley & Sons, New York
- Strobel K., Weber F., Schaab C., Weigel M.K., 1997, *Int. J. Mod. Phys. E* 6, 669
- Strobel K., Weber F., Weigel M.K., 1999, *Z. Naturforsch.* 54a, 83
- Sumiyoshi K., Suzuki H., Toki H., 1995, *A&A* 303, 475
- Takatsuka T., 1995, *Nucl. Phys. A* 588, 365
- Takatsuka T., 1996, *Prog. Theo. Phys.* 95, 901
- Takatsuka T., Nishizaki S., Hiura J., 1994, *Prog. Theo. Phys.* 92, 779
- Thorsett S.E., Arzoumanian Z., McKinnon M.M., Taylor J.H., 1993, *ApJ* 405, L29
- Timmes F.X., Woosley S.E., Weaver T.A., 1996, *ApJ* 457, 834
- Tsuruta S., Cameron A.G.W., 1966, *Can. J. Phys.* 44, 1863
- Van Kerkwijk M.H., van Paradijs J., Zuiderwijk E.J., 1995, *A&A* 303, 497
- Wang C.S., Chung K.C., Santiago A.J., 1997, *Phys. Rev. C* 55, 2844
- Woosley S.E., Weaver T.A., 1995, *ApJS* 101, 181